

AMO's structure and climate footprint in observations and IPCC AR5 climate simulations

**Argyro Kavvada, Alfredo Ruiz-Barradas
& Sumant Nigam**

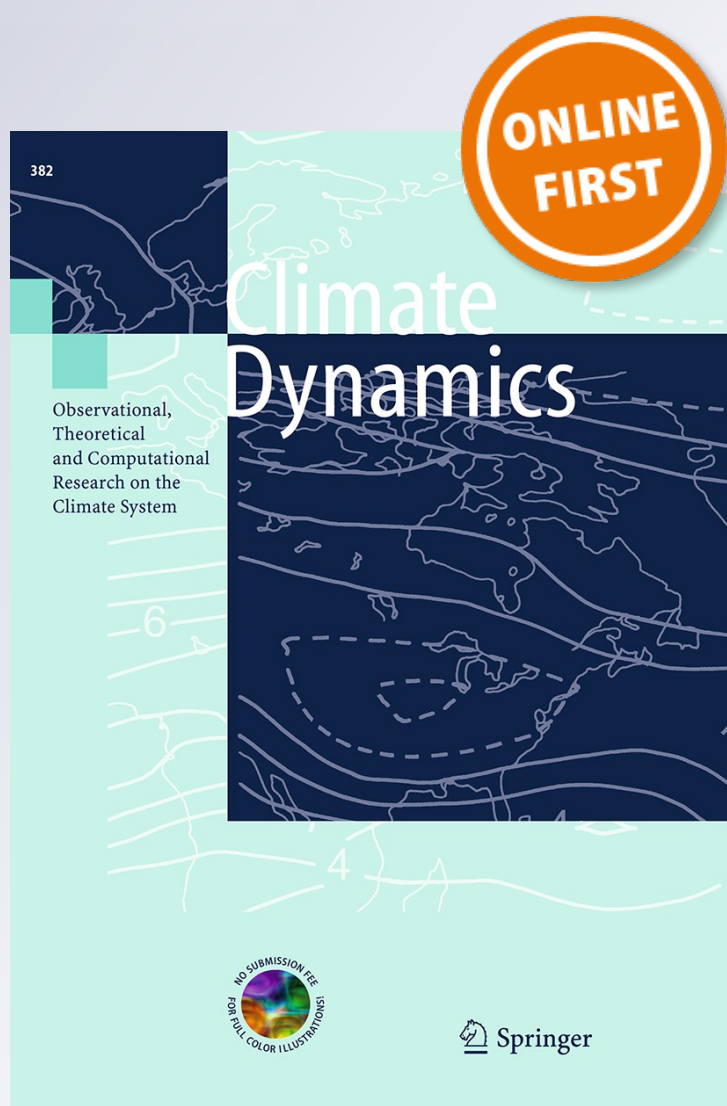
Climate Dynamics

Observational, Theoretical and
Computational Research on the Climate
System

ISSN 0930-7575

Clim Dyn

DOI 10.1007/s00382-013-1712-1



AMO's structure and climate footprint in observations and IPCC AR5 climate simulations

Argyro Kavvada · Alfredo Ruiz-Barradas ·
Sumant Nigam

Received: 4 June 2012 / Accepted: 20 February 2013
© Springer-Verlag Berlin Heidelberg 2013

Abstract This study aims to characterize the spatiotemporal features of the low frequency Atlantic Multidecadal Oscillation (AMO), its oceanic and atmospheric footprint and its associated hydroclimate impact. To accomplish this, we compare and evaluate the representation of AMO-related features both in observations and in *historical* simulations of the twentieth century climate from models participating in the IPCC's CMIP5 project. Climate models from international leading research institutions are chosen: CCSM4, GFDL-CM3, UKMO-HadCM3 and ECHAM6/MPI-ESM-LR. Each model employed includes at least three and as many as nine ensemble members. Our analysis suggests that the four models underestimate the characteristic period of the AMO, as well as its temporal variability; this is associated with an underestimation/overestimation of spectral peaks in the 70–80 year/10–20 year range. The four models manifest the mid-latitude focus of the AMO-related SST anomalies, as well as certain features of its subsurface heat content signal. However, they are limited when it comes to simulating some of the key oceanic and atmospheric footprints of the phenomenon, such as its signature on subsurface salinity, oceanic heat content and geopotential height anomalies. Thus, it is not surprising that the models are unable to capture the majority of the associated hydroclimate impact on the neighboring continents, including underestimation

of the surface warming that is linked to the positive phase of the AMO and is critical for the models to be trusted on projections of future climate and decadal predictions.

Keywords AMO · CMIP5 · Climate models · Historical simulations · Timescale of variability · Hydroclimate impact · Salinity · Ocean heat content

1 Introduction

The planetary-scale mode of sea surface temperature swings in the North Atlantic basin, known as the Atlantic Multi-decadal Oscillation (AMO) after Kerr (2000), has been noted in several past studies (Kushnir 1994; Enfield et al. 2001; Sutton and Hodson 2005; Guan and Nigam 2009; Ting et al. 2009; Frankcombe 2010; Medhaug and Furevik 2011) and has attracted considerable attention in the recent years due to its extensive impact on regional as well as global weather and climate (e.g., Ting et al. 2011). The principal drivers of these basin-wide SST perturbations are, however, unclear and a common consensus with respect to the origin of North Atlantic SST variability remains to be reached. Some of the most prevailing oceanic and atmospheric mechanisms proposed as key drivers of the AMO include density and salinity fluctuations driven by variations in the Atlantic Meridional Overturning Circulation, AMOC (Bjerknes 1964; Latif et al. 2004; Medhaug and Furevik 2011), changes in wind forcing and air–sea interactions (Huang et al. 2011), the secular increase of greenhouse gases such as CO₂, CH₄ etc. (Webster et al. 2005; Mann and Emanuel 2006), as well as fluctuations in atmospheric concentrations of anthropogenic and natural aerosols (Evan et al. 2009; Booth et al. 2012). A question of key significance addresses the issue of

A. Kavvada (✉) · A. Ruiz-Barradas · S. Nigam
Department of Atmospheric and Oceanic Science,
University of Maryland, 3435 Computer and Space Sciences
Bldg., College Park, MD 20742-2425, USA
e-mail: argyrok@atmos.umd.edu

S. Nigam
Earth System Science Interdisciplinary Center,
University of Maryland, College Park, MD 20742-2425, USA

how one can effectively separate the naturally induced, multidecadal North Atlantic SST perturbations from the upward, externally forced, SST trends that are attributed to global warming (e.g., Ting et al. 2009; Guan and Nigam 2009). This along with supplemental, open questions involving the influence of the extra-tropical North Atlantic variability on the signal and evolution of the tropical Atlantic SSTs (the decadal variability of the inter-hemispheric SST gradient across the Equator) and the extent to which these interactions manifest complementary features are the focus of ongoing climate research studies.

Persistent, large-scale SST anomalies exert a meaningful and often predictable influence on climate. AMO's hydroclimate impact on the neighboring continents is thus well anticipated and constitutes a cause of great concern, due to the large timescale of the phenomenon and its remarkable socioeconomic effects. Impacts on the regional surface climate associated with the AMO include droughts over North America (Sutton and Hodson 2005; Nigam et al. 2011), decreased rainfall over the Sahel and changes in the frequency and intensity of North Atlantic hurricanes (Knight et al. 2006; Zhang and Delworth 2006; Enfield and Cid-Serrano 2006, Ting et al. 2009; Guan and Nigam 2009) as well as decadal variations in surface air temperature over NE Brazil (Knight et al. 2006) and parts of Northern Europe.

Apart from the atmospheric response, multidecadal variability in the North Atlantic climate system also exhibits a signature on subsurface oceanic heat content and salinity, as well as on Arctic sea ice. As noted in several studies, the North Atlantic Ocean presents an extensive record of perturbations involving SST and salinity (Reverdin et al. 1997; Zhang and Vallis 2006; Polyakov et al. 2005a, b) as well as sea ice anomalies (Deser and Blackmon 1993; Deser et al. 2002). Fresh water anomalies (reduced salinity) over the Labrador Sea, a region of deepwater formation, stratify the ocean layer, contributing thus to the weakening of the thermohaline circulation and deep water formation. This allows for the layer to cool down due to the lack of vertical mixing with the warmer subsurface water, which in turn and via a positive feedback, inhibits further the deep convection due to a reduction in the heat lost to the atmosphere (Gelderloos et al. 2012).

Furthermore, most of Earth's warming signal stemming from human forcing resides in the upper ocean (Hansen et al. 2005; Levitus et al. 2005). That is not to say that temperature anomalies in the deeper (1,000–3,000 m) layer below the sunlit zone are not important for climate variability on a global scale, but that their contribution to the net integral of ocean heat content is small, when compared to that of the upper ocean (Levitus et al. 2000). The oceanic heat content acts as a key indicator of climate perturbations on seasonal, interannual and longer time scales (e.g., Chu 2011; Lozier et al. 2008), accounting for the total amount

of heat that is made available to the atmosphere, via heat transport (i.e., surface heat fluxes that dominate variability on seasonal and annual timescales) and heat storage (Kelly and Dong 2004). Examining, thus, the spatial and temporal patterns of sub-surface temperature and ocean heat content is essential in understanding regional warming trends and relating them to low-frequency modes of climate variability. The evolution and respective changes between surface and sub-surface temperature and salinity is also a strong fingerprint of decadal fluctuations in the oceanic overturning circulation (AMOC) and can thus provide significant insight on the vertical structure of the AMO (Zhang 2007) and its linkage to meridional density and salinity transport processes (Sundby and Drinkwater 2002). Assessing such long-term variability, however, can be challenging due to the short record of sub-surface data that is available, in relation to the extensive variability timescale (Keenlyside et al. 2008).

Advancing our ability to identify the principal drivers and impacts of the AMO, and the relative roles of anthropogenic and natural contributions to AMO's spatio-temporal evolution can therefore facilitate (1) the formulation of a more refined image of the North Atlantic SST variability and its local and remote climate influences and (2) the accuracy and reliability of climate model projections of future trends. Achieving these goals, however, remains a challenge; proxy data (ice-core records, tree rings etc.) and climate simulations with models of varied complexity (e.g., Frankcombe 2010; Hodson et al. 2010) offer supplemental tools for improving our understanding of such low frequency, planetary-scale interactions. A holistic image of the AMO and its climate impacts, as well as its accurate representation in climate simulations is yet to be reached, however.

In this study, the structure and evolution of the Atlantic Multidecadal Oscillation have been investigated in observations and model simulations of the twentieth century climate from models participating in the CMIP5 project (Taylor et al. 2012). We have sought to identify ways in which the spatiotemporal evolution of North Atlantic SSTs that are associated with the AMO compares between models and observations, while also constructing a 3-dimensional image of its structure, by examining decadal-scale perturbations on the North Atlantic surface, subsurface, as well as the overlying atmosphere.¹ Some of the central questions that have been addressed include:

¹ The use of coupled, ocean–atmosphere models from the CMIP5 project allows for the ocean circulation to freely evolve, facilitating, in this way, a more accurate understanding of the AMO-related ocean state and its imprint on local as well as remote climate features. A downside of this approach, however, is that in such models, there are so many fields that are varying simultaneously, that it becomes very challenging to separate cause from effect.

- How robust is the AMO structure and how does it evolve through time (i.e., how coherently does it evolve in space and time)?
- Is the AMO associated with deep, coherent salinity and heat content anomalies?
- How do simulations from four state-of-the-art global climate models participating in the CMIP5 project portray the observed features of the AMO and its surface climate impact?

The paper is organized as follows. A description of the observational datasets, the coupled ocean–atmosphere models and their simulations from the CMIP5 project is provided in Sect. 2, along with some working definitions employed in this study; the AMO structure at the surface, its time signature and its evolution in observations and simulations of the twentieth century climate are presented in the following section, while Sect. 3.2 reviews the associated subsurface salinity and temperature features; the atmospheric response to the AMO and its climate impact are reviewed in Sect. 3.4; a summary and concluding remarks are given in Sect. 5.

2 Data and analysis methods

2.1 Data

To investigate the structure, properties and impacts of the AMO, we used a variety of observational variables including sea surface temperature (SST), sub-surface potential temperature and salinity, as well as geopotential height, surface air temperature and precipitation. The SSTs were obtained from the Met Office's (UKMO) Hadley Centre Sea Ice and Sea Surface Temperature dataset, HadISST version 1.1 (Rayner et al. 2005), available on a $1^\circ \times 1^\circ$ grid at a monthly resolution for the 1870–present period. Both subsurface temperature and salinity fields were obtained from the National Oceanographic Data Center (NODC) (Levitus et al. 2001) and the SODA Ocean Reanalysis product, version 2.2.4 (Carton et al. 2005). The NODC dataset included subsurface temperature anomalies on a $1^\circ \times 1^\circ$ horizontal grid with 26 vertical levels (sfc.–2,000 m) at seasonal resolution for the winter 1955–fall 2010 period. NODC subsurface salinity measurements were provided as 5-year (pentadal) averaged anomalies (Boyer et al. 2005) at annual resolution on a $1^\circ \times 1^\circ$ horizontal grid and with 26 vertical levels, for the period 1955–2006. The SODA 2.2.4 dataset was provided at a $0.5^\circ \times 0.5^\circ$ horizontal grid with 40 vertical levels, at monthly resolution for the period between January 1871 and December 2008. Geopotential height data were obtained from the National Center for Environmental

Table 1 Ensemble members used for Figs. 1, 2, 3, 7 and 8

IPCC CMIP5 twentieth century models	Runs used
GFDL-CM3	1, 2, 3, 4, 5
CCSM4	1, 2, 3, 4, 5, 6
ECHAM6/MPI-ESM-LR	1, 2, 3
UKMO-HadCM3	1, 2, 3, 4, 5, 6, 7, 8, 9

The bold numbers indicate the model runs that were used for the remaining Figs. 4, 5, and 6

Prediction (NCEP) Reanalysis (Kalnay et al. 1996) at a horizontal resolution of $2.5^\circ \times 2.5^\circ$ and with 17 vertical levels, at monthly resolution for the January 1949–December 2009 period. Finally, we obtained precipitation and surface air temperature data from the CRU TS3.1 monthly data set (Mitchell and Jones 2005), available over land points at a $0.5^\circ \times 0.5^\circ$ resolution for the January 1901–October 2009 period.

Models from the CMIP5 project that we used to analyze the twentieth century climate simulations included those from leading climate research centers around the world: NCAR's CCSM4 (6 ensemble members), NOAA's GFDL-CM3 (5 ensemble members), UK Meteorological Office's UKMO-HadCM3 (9 ensemble members) and the German Max Planck Institute's ECHAM6/MPI-ESM-LR (3 ensemble members). For most models, the historical simulation scenario covered the period 1850/1860–2005. The time varying forcing agents that were employed included emissions or concentrations of natural and anthropogenic aerosols (or their precursors), solar forcing, greenhouse gases (CO_2 , CH_4 , N_2O), atmospheric composition as well as land use change (Meinshausen et al. 2011). Table 1 shows the model simulations (ensembles) that were used (based on availability at the time) for the analysis of the different oceanic and atmospheric, AMO-related fields.

2.2 Methods

The current analysis aimed at documenting the spatio-temporal characteristics and evolution of the observed and modeled low frequency AMO pattern, along with its impact on various seasonal resolution fields for the period 1900–1999. Seasonal averages of the different monthly variables were calculated based on the usual Northern Hemisphere meaning of the three-month season average: December–February for winter, March–May for spring, June–August for summer and September–November for fall. Seasonal anomalies of the different fields were calculated by subtracting the seasonal climatology (i.e., the long-term mean using the 1900–1999 base period, unless noted otherwise) from the seasonal fields. Observed and simulated AMO indices were created by taking the

following steps: a. constructing the observed and simulated AMO indices by first averaging the respective seasonal SST anomalies (SSTA) over the Atlantic region (5° – 75° W, 0° – 60° N),² and subsequently, linearly de-trending them over the January 1900–October 1999 period, using the least-squares method, b. smoothing these indices by applying a binomial (1-2-1) filter 50 times to efficiently remove interannual variations without aliasing the decadal-scale pulses and c. normalizing the de-trended and smoothed time series to unit variance, by dividing each time series by the respective standard deviation of the calculated index. Finally, indices for a specific season were created by extracting that season from the all-season, smoothed and normalized index.

Lead/lag regressions of the all-season (derived from step a.) AMO indices on the different field variables were calculated for both observational and model-generated data. Regressions from model simulations were computed for each ensemble member of a given model, separately, and a mean value of the combined regression results was subsequently obtained and shown (rather than demonstrating the regressions on the mean ensemble field of a given model).

It should be noted that the defined seasons for the provided temperature anomalies from NODC were calculated in a slightly different way, in comparison to the ones from other datasets that were used in this analysis: January–March was used for winter, April–June for spring, July–September for summer and October–December for fall. Finally, since the NODC salinity anomalies were given at annual resolution, we linearly interpolated this dataset in time, to create its seasonal version. Despite the fact that this technique did not produce meaningful seasonal values and it wasn't thus optimal for researching the time evolution or spatial footprint on a particular season, it allowed the investigation of all-season, contemporaneous salinity regressions and latitudinal salinity profiles (seasonal differences were leveled out in this case.)

3 Results

3.1 Observed versus modeled, spatiotemporal features of the AMO

Climate simulations of the twentieth century constitute a real challenge for the models, since they largely depend on their ability to simulate natural variability given the

relatively modest role of the observed GHG and aerosol forcing that is being used (in comparison with the twenty-first century, forced projections). Thus, a first-order question that one can ask is whether the models possess the necessary elements to portray the characteristic, basin-wide SST anomalies that relate to the AMO. The structure of the SST anomalies associated with the warm phase of the AMO in observations and simulations is shown in Fig. 1, via simultaneous all season regressions. Positive anomalies are present over the entire North Atlantic basin in observations, with maximum values of as high as 0.4 K arising just south of Greenland in the mid-latitudes, between 40° and 50° N and 35° to 45° W and with a secondary maximum (half the size of the one over the mid-latitudes) noted over the northern tropical Atlantic, off of the coast of northwest Africa; normal conditions are evident in the western subtropical latitudes.

The four models capture the general spatial structure of the SST anomalies as portrayed in observations, with some clear differences, however. Most models exhibit a region of positive anomalies in the mid-latitudes, while placing the maximum of the anomalies further to the east (southeastward of Greenland) than observations show; furthermore, the models also exhibit weaker positive anomalies over the Davis Strait and the Labrador Sea, while also showing a weaker secondary maximum off of the northwestern African coast, in comparison to observations. It is interesting to note that GFDL-CM3 is the only model that portrays the same anomalies over the Labrador Sea as seen in observations, with the subtropical/tropical extension of the anomalies appearing further to the west; anomalies are also shown over the equatorial Pacific, a feature not present in observations. On the other hand, anomalies in CCSM4 are constrained to the northern latitudes, with two local maxima southward of Iceland and over the Greenland Sea, but with normal conditions off of the northwest African coast. Similarly to GFDL-CM3, CCSM4 demonstrates anomalies over the equatorial Pacific that are not present in observations. Anomalies over the N. Atlantic mid-latitudes from ECHAM6/MPI-ESM-LR and UKMO-HadCM3 appear weaker and stronger, respectively, in comparison to observations. In addition, the latter two models appear unable to capture the magnitude of the observed anomalies in the subtropical/tropical Atlantic, with UKMO-HadCM3 being closer to observations than ECHAM6/MPI-ESM-LR.

After investigating the spatial structure of the AMO at the surface, we now concentrate on the propagation of its spatial footprint through time. For this purpose, we compare the time series of the observed and model-based AMO indices for the January 1900–October 1999 period, while choosing to display the AMO time series of the ensemble member (of each model) that manifests the highest correlation with observations (Fig. 1, bottom panel.). The AMO

² Note the similarity in the domain used to define the area-averaged SST anomalies by Sutton and Hodson (2003) (7.5° – 75° W, 0° – 60° N), as well as the difference in the way of smoothing the area-averaged SST anomalies, via the use of a 37-point Henderson filter.

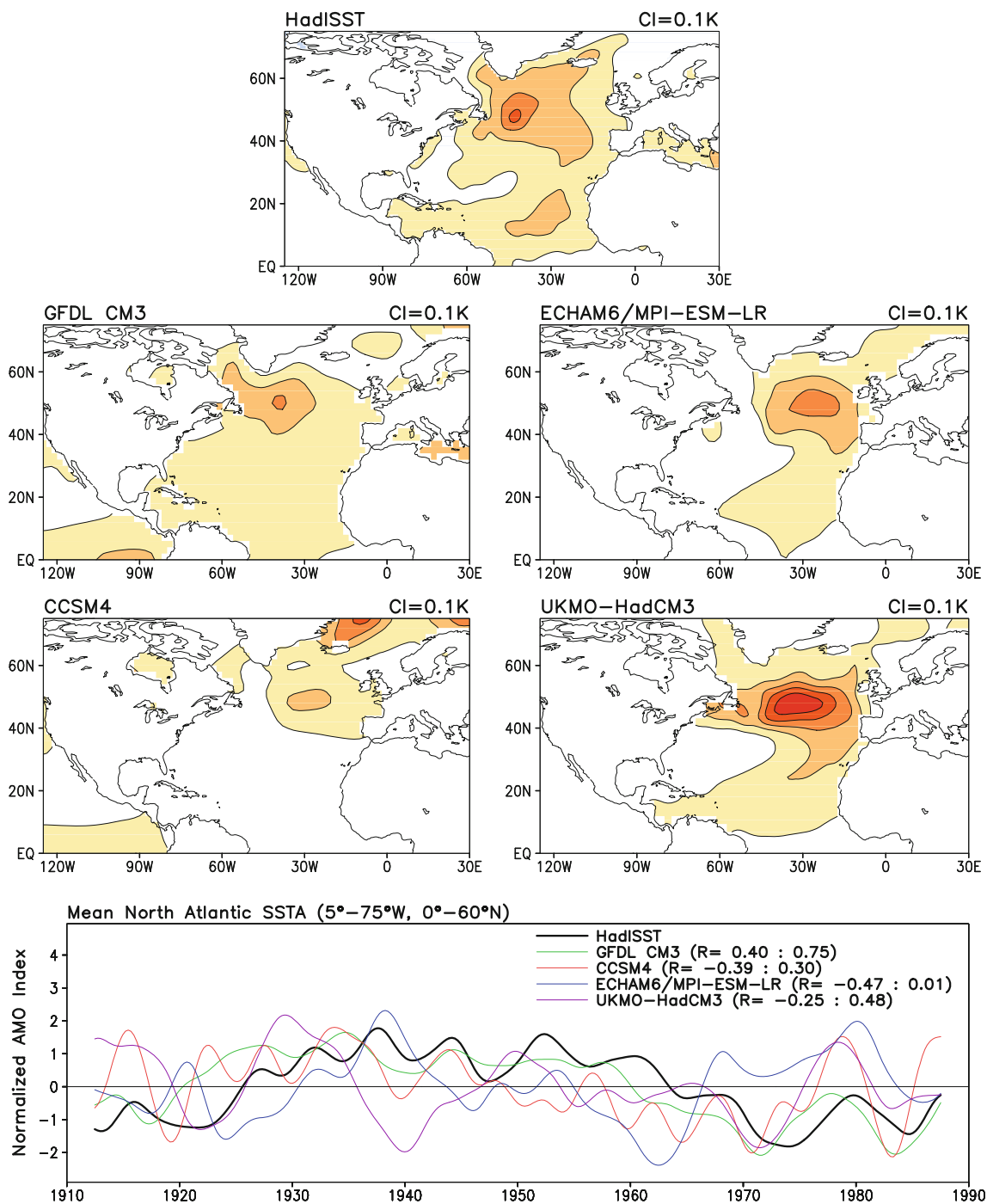


Fig. 1 All-season regressions of standardized smoothed AMO indices on SSTs for the winter 1900–fall 1999 period. Regressions for the models are calculated for each ensemble member separately and then an average is computed for each model. *Red/blue* shading denotes positive/negative SST anomalies; contour interval is 0.1 K. The indices are constructed by first calculating a spatial average of SST anomalies over the (5°–75°W, 0°–60°N) region and then detrended, using the least squares method. The indices are finally smoothed by applying a 1-2-1 binomial filter 50 times and normalized by using

their standard deviation. Regressions are shown after 5 applications of smth9 in the GRADS plotting software. *Bottom Panel* Observed HadISST smoothed AMO index and other four model-derived smoothed AMO indices which have the highest correlations, R, with the observed index: GFDL-CM3, Ensemble 5 (R = 0.75), UKMO-HADCM3, Ensemble 4 (R = 0.56), ECHAM6/MPI-ESM-LR, Ensemble 3 (R = 0.01) and CCSM4 Ensemble 4 (R = 0.29). The correlation range for the different ensembles within each model is shown adjacent to the model's name

Table 2 Correlations of the smoothed AMO indices between model simulations of the twentieth century climate and the observed smoothed AMO index for the period 1900–1999

IPCC AR5 twentieth century simulations	Run 1	Run 2	Run 3	Run 4	Run 5	Run 6	Run 7	Run 8	Run 9
GFDL-CM3	0.40	0.51	0.49	0.56	0.75	–	–	–	
CCSM4	0.14	0.14	–0.39	0.29	–0.03	–0.18	–	–	
ECHAM6/MPI-ESM-LR	–0.47	–0.1	0.01	–	–	–	–	–	
UKMO-HadCM3	0.38	0.36	–0.23	0.11	0.48	0.23	–0.14	0.39	0.29

The statistical significance of the regressions is assessed via a two-tailed Student's *t*-test at the 5 % level, using an effective sample size $N_e = 25$ (degrees of freedom). Critical correlation is found to be (R_c) equal to **0.38**. Correlations above this value are statistically significant

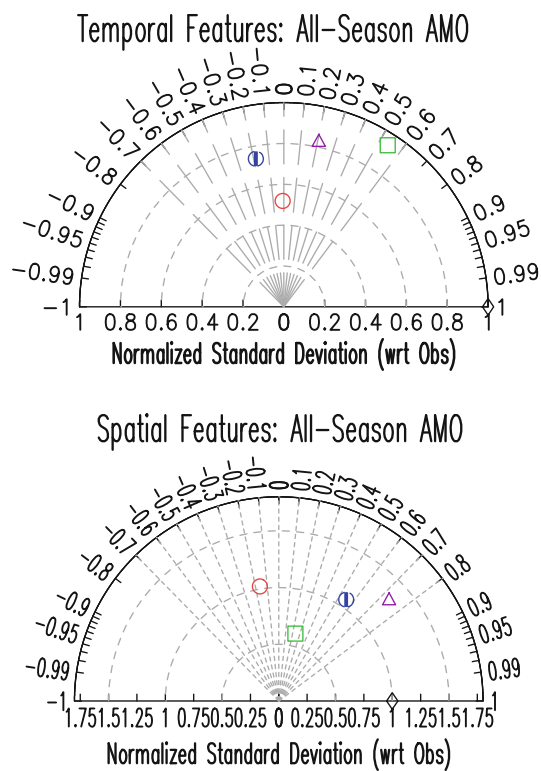
index from GFDL-CM3, Run 5, is the closest to the observed index, with a simultaneous correlation of 0.75. This is followed by the AMO index from UKMO-HadCM3, Run 5, with a 0.48 correlation, and the index from CCSM4, Run 4, with a correlation of 0.29. Finally, the AMO index from ECHAM6/MPI-ESM-LR, Run 3, shows the least co-variability with observations, with a maximum correlation of 0.01. All correlation coefficients for the ensemble members of each model are shown in Table 2. The statistical significance of the correlations is assessed via a two-tailed Student's *t* test at the 5 % level using an effective sample size that accounts for serial correlation (Quenouille 1952), $N_e (=N/[1 + 2r_{x,1}r_{y,1} + 2r_{x,2}r_{y,2} + \dots])$, where N is the time-series length (here 300 seasons after the smoothing); $r_{x,1}, r_{x,2}, \dots$ are the first, second, ...-order autocorrelations for the observed time series (x), and $r_{y,1}, r_{y,2}, \dots$ are the corresponding first, second, ...-order autocorrelations for the time series of each ensemble member of each model ensemble mean (y); stable N_e (and thus *t* test) values are obtained by summing up to the 6th-order. The degrees of freedom corresponding to the ensemble mean for all four models are found to be in the 24–26 range so a value of 25 was used. Based on this analysis, the critical correlation is subsequently calculated via the formula: $t = r^* \sqrt{\frac{N_e}{1-r^2}}$ and is found to be ± 0.38 . Correlations above this value are considered statistically significant.

Supplemental information regarding the spatial and temporal features of the smoothed AMO indices derived from observations and the ensemble means of the four models is found in Fig. 2, via the use of Taylor diagrams (Taylor et al. 2012). Comparison of the temporal features of the AMO indices indicates that the majority of the models have poor correlation with observations and under-estimate the observed variability, with the exception of GFDL CM3, which shows a slightly above 0.5 correlation to observations and a standardized, standard deviation of ~ 0.94 . Regarding the spatial variability and spatial correlations between the observed and modeled SST anomalies of the mature phase of the AMO, UKMO-HadCM3 is the best among the four models in depicting AMO's observed, spatial structure, with a correlation of

0.74, followed by MPI-ESM-LR and GFDL CM3, with correlations of 0.55 and 0.24, respectively. CCSM4 is the least efficient in capturing the spatial structure and variability of the AMO, with temporal and spatial correlations of -0.01 and -0.16 , respectively. To resume, UKMO-HadCM3 and MPI-ESM-LR seem to be most efficient in capturing the spatial features of the mature phase of the AMO, whereas GFDL CM3 appears to be the best model in capturing AMO's temporal structure and variability.

Next, we focus on the time scale of the AMO indices, by looking at their autocorrelation functions (Fig. 3). The time span defined by the crossing of the autocorrelation line of the AMO index with the zero line at both ends indicates the half-period of the AMO index.³ The crossing of the autocorrelation of the observed AMO index with the zero line (thick black line) shows a dominant period of approximately 58 years. The color lines, representing the mean autocorrelation for each model, display varying amplitudes and a general underestimation of the AMO period. These appear to be relatively close together, particularly the ones corresponding to UKMO-HadCM3, CCSM4 and GFDL-CM3 models, with periods of 52, 50 and 48 years, respectively (looking at the zero line crossing); the ECHAM6/MPI-ESM-LR autocorrelation function demonstrates the shortest period (40 years). An estimate of the observed and model-based AMO periods is shown in Table 3. It is interesting to point out that while the characteristic time of the AMO indices by the models is up to 31 % apart from the observed value when considering the zero crossing metric, it is further apart (within 65 % of the observed value) when considering the time needed for the autocorrelations to decay to $1/e$ of their values, a measure of the memory or persistency of the AMO. Graphically, this suggests that higher frequency variability remains present in the model indices, in contrast to the observed AMO index. Spectral analysis of the smoothed AMO

³ That is, the time it takes for the anomaly to grow from climatological conditions to reach its maximum value and then go back to climatological conditions before going in the opposite direction.



□ GFDL-CM3(5), ○ CCSM4(6), △ UKMO-HadCM3(9), ◆ MPI-ESM-LR(3)

Fig. 2 Taylor diagrams of smoothed AMO indices and their regressions from observations and CMIP5 climate model simulations for the period 1900–1999. Normalized standard deviations, correlations and standard deviations are calculated between observations and the different ensembles' mean for each model, to compare the temporal and spatial variability and correlations between observations and the four models. The temporal (spatial) standard deviations are normalized with respect to the observed, temporal (spatial) standard deviation of 0.17 K (0.46 K). The horizontal (x axis) shows normalized standard deviation values, whereas the arc-part of the diagrams shows the respective correlation values. Each model is shown in a *different color* (see legend) and the *number in parenthesis* denotes the number of ensembles used from each model to generate the mean standard deviation and mean correlation

indices is displayed in Fig. 4 (histograms of the spectral peaks, derived from the mean spectral peaks of the different model ensembles are shown in 10-year bins). The observed smoothed AMO index (Fig. 4) reveals a spectral peak in the 70–80 years range, which is four times larger than the peak in the 10–20 years range. However, the mean spectral peaks in the 10–20 years range of the smoothed indices from model simulations have a more prominent role than their corresponding 70–80 year peaks (and than the ones seen in observations); in fact, these higher frequency peaks are comparable to (actually slightly larger than) their 70–80 year peaks. This helps explain why the peaks displayed in the autocorrelation of the indices in Fig. 3 are so narrow.

An additional insight with respect to the models' skill to simulate low-frequency variability over the North Atlantic Ocean associated with the AMO is investigated by the evolution of the SST anomalies associated with the AMO via all-season lead/lag regressions, 4 years before and after the mature phase of the AMO (Fig. 5). Observations indicate that positive SST anomalies emerge from the Davis Strait and Labrador Sea following a southeastward propagation in the higher mid-latitudes and a subsequent southwestward advection in the lower latitudes, as time evolves, tracking the east branch of the subtropical gyre until they reach maximum amplitude and extension in the mature phase. The subtropical anomalies appear weaker than those in the mid-latitudes, with a local maximum developing off of Northwest Africa. In the post-mature phase, the anomalies gradually abate, with the signal first dissipating over the tropical latitudes and subsequently further to the north. Positive anomalies over the North Pacific appear more extensive in the SODA-based AMO evolution than in the HadISST dataset.⁴

The modeled AMO structure and evolution around the mature phase of the AMO (± 4 years) agrees partially with observations, particularly in the mid-latitudes just before and after the mature phase (± 2 years). Noticeable differences are present, however, in the CCSM4 evolution, which manifests a focus on the northern North Atlantic over the Greenland Sea that is not present in observations; furthermore, GFDL-CM3 and ECHAM6/MPI-ESM-LR show negative anomalies at the end of the +4 years lag period, a feature that is also not present in observations. Except for CCSM4, anomalies in the other three models reach maximum latitudinal extension into the tropics in the mature phase; GFDL-CM3 and UKMO-HadCM3 exhibit a greater ability in capturing AMO-related anomalies in the tropical North Atlantic, which remains almost completely quiescent in the other two models, during the pre- and post-mature phases (in contrast to observations). It can therefore be inferred that even though the models do capture the northward focus of the observed SSTA maxima, they lack the ability to effectively reproduce their structure and evolution, especially over the tropical part. The quick setting and dismissal of the simulated tropical SST anomalies may be related to the superficial nature of the anomalies, with little consideration of subsurface processes, in the models.

⁴ To investigate this difference, we used NOAA's Extended Reconstructed SST data set (ERSSTv3b, Smith et al. 2008) to generate a smoothed AMO index and lead/lag SST regressions (not shown); the emerging pattern agrees with the lead/lag regressions from HadISST, with SST anomalies over the Pacific being less widespread than the ones noted in the SODA lead/lag regressions.

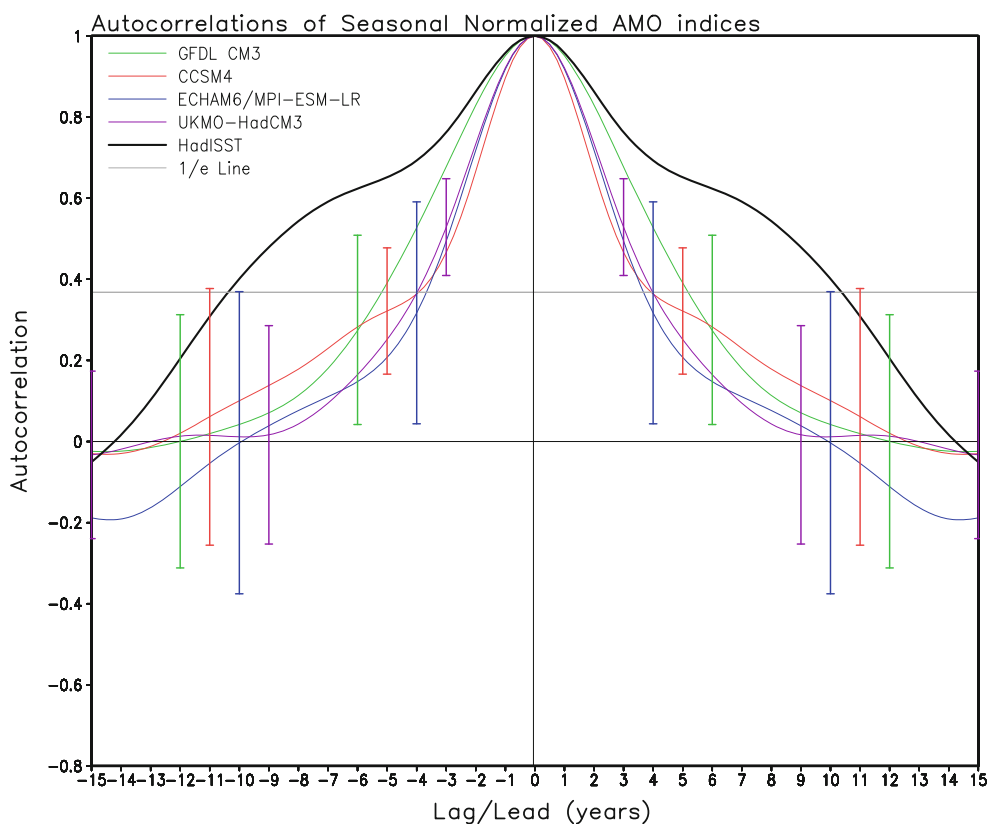


Fig. 3 Standardized smoothed AMO indices are calculated for each ensemble member of each model; subsequently, their corresponding autocorrelations are calculated and a mean autocorrelation is finally computed and displayed. Autocorrelations are calculated for $t - 15$ to $t + 15$ years and compared to the autocorrelation time series derived

from observations (*black line*). The standard deviation (SD) error bars among the different autocorrelations are also calculated and drawn here, to indicate the dispersion of the individual ensemble autocorrelations for each model from the ensemble mean

Table 3 Timescale in years of the smoothed AMO indices estimated from their autocorrelation functions displayed in Fig. 2

Model/Obs	Zero-crossing	1/e-crossing
Observations	58	44
GFDL CM3.1 (4 runs)	48	22
CCSM4 (6 runs)	50	16.5
ECHAM6 (3 runs)	40	15.5
HadCM3 (9 runs)	52	16.5

If considering the anomalies of a given sign decay until the autocorrelation reaches a certain value, this defines a quarter of the period of the phenomenon. If the zero line is used to define the period of the smoothed AMO index, its period is given in the zero-crossing column, but if the 1/e line is used instead, the period is given under the 1/e-crossing column

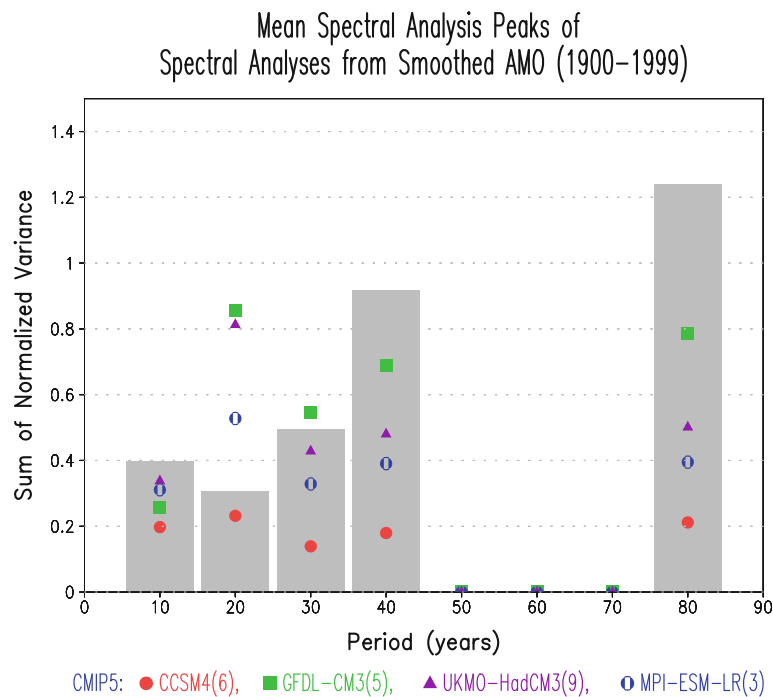
3.2 Subsurface features of the AMO: salinity

The identification of footprints of low-frequency variability of North Atlantic SSTs on ocean surface and sub-surface fields is essential for the construction of a more holistic image of the AMO. The current study focuses on the sfc-50 m oceanic layer in an attempt to assess the spatial

distribution, magnitude and vertical structure of any AMO-related salinity anomalies during the winter 1955–fall 1999 period, which is common among observations and model simulations. The AMO indices are re-calculated for this shorter period (by using NODC, SODA and simulated SST fields, respectively, Fig. 6).

The regressed observed SST anomalies from the 1955 to 1999 period (Fig. 6, left column, upper two panels) display only a small variation in their structure, when compared with those of the larger period (Fig. 1), with slightly weaker/stronger anomalies over the mid/tropical Atlantic and almost normal conditions over the subtropical western Atlantic (off of the eastern US coast). Negative anomalies are now discernible, north of the Greenland Sea. The associated anomalies over the Atlantic mid-latitudes appear of the same magnitude to the ones over the tropics. The simulated anomalies for this shorter period retain their spatial structure, as seen in the longer period, but are unable to capture the extension and magnitude of the cold anomalies off of the US coast as well as the increase in magnitude of the anomalies over the tropical Atlantic. Except for GFDL-CM3, the other three, simulated

Fig. 4 Histogram of mean spectral analysis' peaks from smoothed AMO time series. A histogram of the dominant frequency peaks derived from a spectral analysis of the mean smoothed, AMO indices derived from the four models are shown for the January 1900–October 1999 time period. The sum of normalized variance is shown on the y axis and the dominant periods in years are shown on the x-axis. The dominant frequencies for each model are shown in *different colors* (see legend) and the *number in parenthesis* denotes the number of ensembles used from each model to generate the mean spectrum (corresponding to the mean, model-derived AMO time series.)



regressed anomalies are of smaller magnitude, in comparison to the longer period ones. (Fig. 6, left column, lower four panels).

Regressed salinity anomalies are analyzed as a vertical mean along the sfc-50 m layer (Fig. 6, central column) and as a vertical profile (Fig. 6, right column). Contained, positive, vertically-averaged (sfc-50 m) salinity maxima are noted in observations in the mid-latitudes, south of Greenland (Fig. 6, central column, upper two left panels), while negative values are evident in NODC along the northeastern US coast. We note that the negative salinity anomalies in NODC agree with the observed, negative SST anomalies, a co-occurrence absent from the SODA-derived regressions. Negative salinity anomalies are also found in the western northern tropical Atlantic, between the Equator and 25°N, while positive anomalies are discernible over the Davis and Fram Straits as well as over the Labrador and Greenland Seas, in both NODC and SODA datasets.

The latitudinal profile of the regressed salinity anomalies along the 35°–50°W band in the upper 50 m indicates a coherent vertical structure (Fig. 6, right column, upper two panels). The observed contrasting anomalies identified in the vertical average (south of Greenland and in the northern tropical Atlantic) extend into the subsurface. It is worth noting that lead/lag regressed salinity anomalies (not shown) indicate a counterclockwise propagation of sub-Arctic water into the North Atlantic, from the Davis Strait extending southward into the Labrador, Greenland and Norwegian Seas. Such decadal pulses are evident in past incidents of low salinity and sea surface temperature

anomalies in the region, such as the Great Salinity Anomaly of 1968–82 (Slonosky et al. 1997). Our analysis, hence, supports the notion that N. Atlantic surface temperature and salinity show coherent, low frequency fluctuations, which are consistent with heat and freshwater interactions between the Arctic and the N. Atlantic basins (Polyakov et al. 2005a, b).

Mean regressed positive salinity anomalies from the four models (Fig. 6, central column, four lower panels) are reminiscent of the regressed SST positive anomalies that have already been analyzed (Fig. 6, left panels). While GFDL-CM3, ECHAM6/MPI-ESM-LR and UKMO-HadCM3 exhibit maximum positive salinity anomalies over the regions of maximum SST positive anomalies in the mid-latitudes, CCSM4 manifests negative anomalies, with only hints of a positive signal off of the southwestern tip of Greenland; anomalies over the subtropical region off of the northwest African coast are portrayed in different ways by all four models. GFDL-CM3 captures the extent and spatial variability of AMO-related salinity anomalies, while exaggerating, however, their magnitude; prominent positive anomalies are evident south of Greenland, along with negative anomalies off of the northeastern US (seen in the NODC map) and off of the northwestern African coast. ECHAM6/MPI-ESM-LR and UKMO-HadCM3 depict salinity maxima slightly displaced eastward (in comparison to the observations). Finally, none of the models is able to simulate the positive salinity anomalies over the Straits around Greenland (from the NODC and SODA maps).

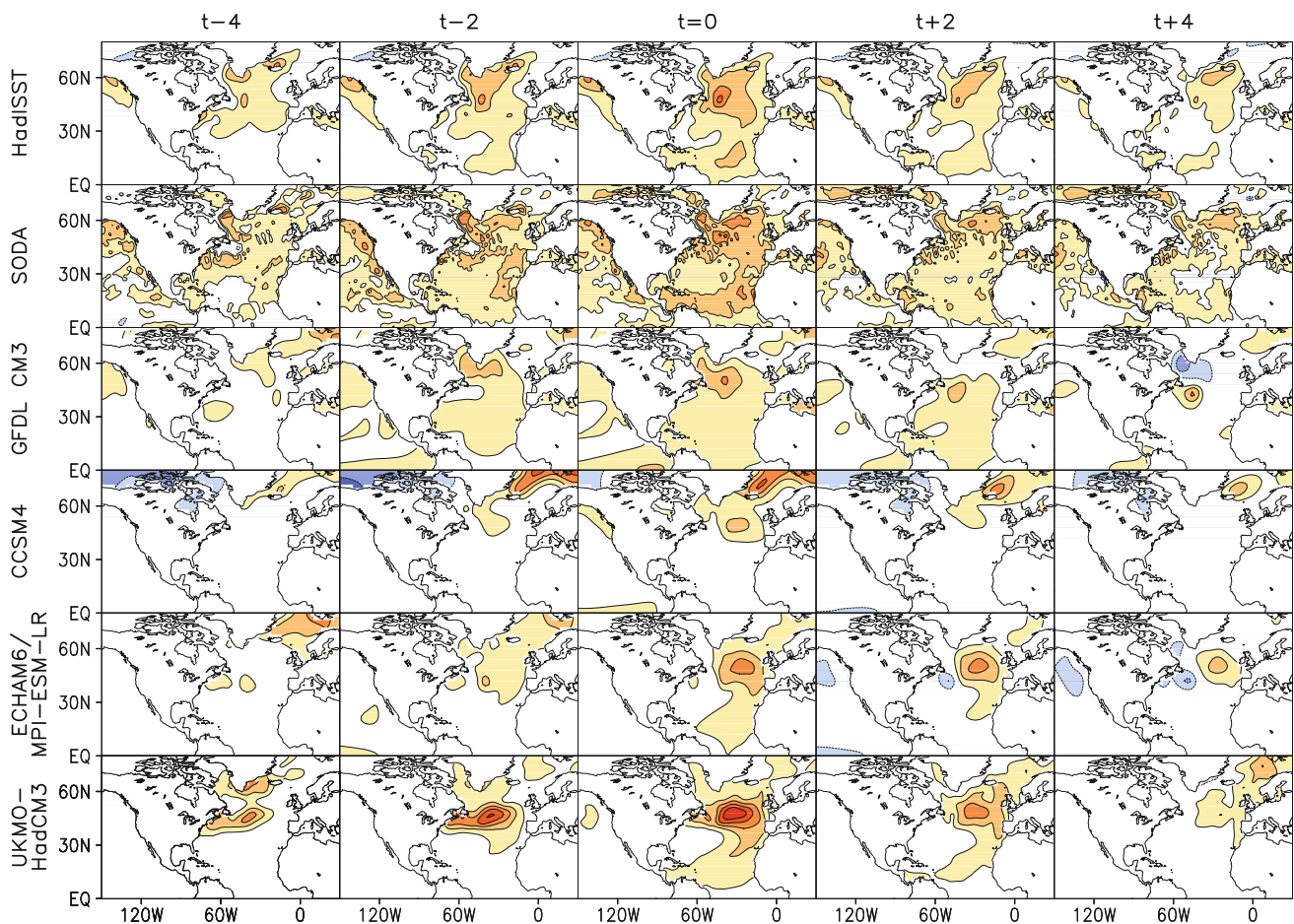


Fig. 5 All-season lead/lag regressions of the smoothed AMO indices on SSTs for the winter 1900–fall 1999 period: SST anomalies are shown 4 years before and after the mature phase: pre-mature conditions are shown 4 years ($t - 4$ column) and 2 years ($t - 2$ column) before the mature phase (t column), while post-mature conditions are shown 2 years ($t + 2$ column) and 4 years ($t + 4$ column) after the mature phase. The *upper two rows* show regression anomalies from observations by HadISST and by the SODA 2.2.4

ocean reanalysis. The *remaining rows* show the related AMO SST anomalies from model simulations of the twentieth century climate from GFDL CM3, CCSM4, ECHAM6/MPI-ESM-LR and UKMO-HadCM3. Regressions are calculated for each ensemble member separately and a mean regression is subsequently computed. *Red/blue* shading denotes positive/negative anomalies; contour interval is 0.1 K. Regressions are shown after 5 applications of the *smth9* function in the GrADS plotting software

The salinity profiles from the model simulations (Fig. 6, four lower right panels) show that the profile from the GFDL-CM3 model is the closest to the observed one, even though it manifests mid-latitude negative anomalies that are not present in observations. Salinity profiles from CCSM4 and ECHAM6/MPI-ESM-LR are in the least agreement with observations, despite the fact that they demonstrate a coherent salinity structure through the sfc-50 m layer. On the other hand, the salinity profile from UKMO-HadCM3 does not show any resemblance to the observed profiles and is characterized by negative salinity anomalies underneath the positive ones, in the mid-latitudes. In short, the models appear challenged in portraying the position and magnitude of AMO-related, salinity anomalies, with GFDL-CM3 being the most successful in capturing the spatial variability of the SSTA-associated, salinity field.

3.3 Subsurface features of the AMO: ocean heat content

As mentioned in the Introduction, heat content has been identified as an important marker in climate variability studies. It is therefore important to examine some of the directly observable sub-surface signatures of the AMO, such as the sub-surface temperature and oceanic heat content.

Subsurface temperatures from NODC, SODA and model simulations are used to obtain vertically integrated heat content anomalies for the sfc-400 m layer. Figure 7 shows lead/lag regressions of the AMO on the oceanic heat content 4 years before and after its mature phase, at 2-year intervals. It is worth noting the coincidence of the anomalies between the NODC and SODA datasets. Four years

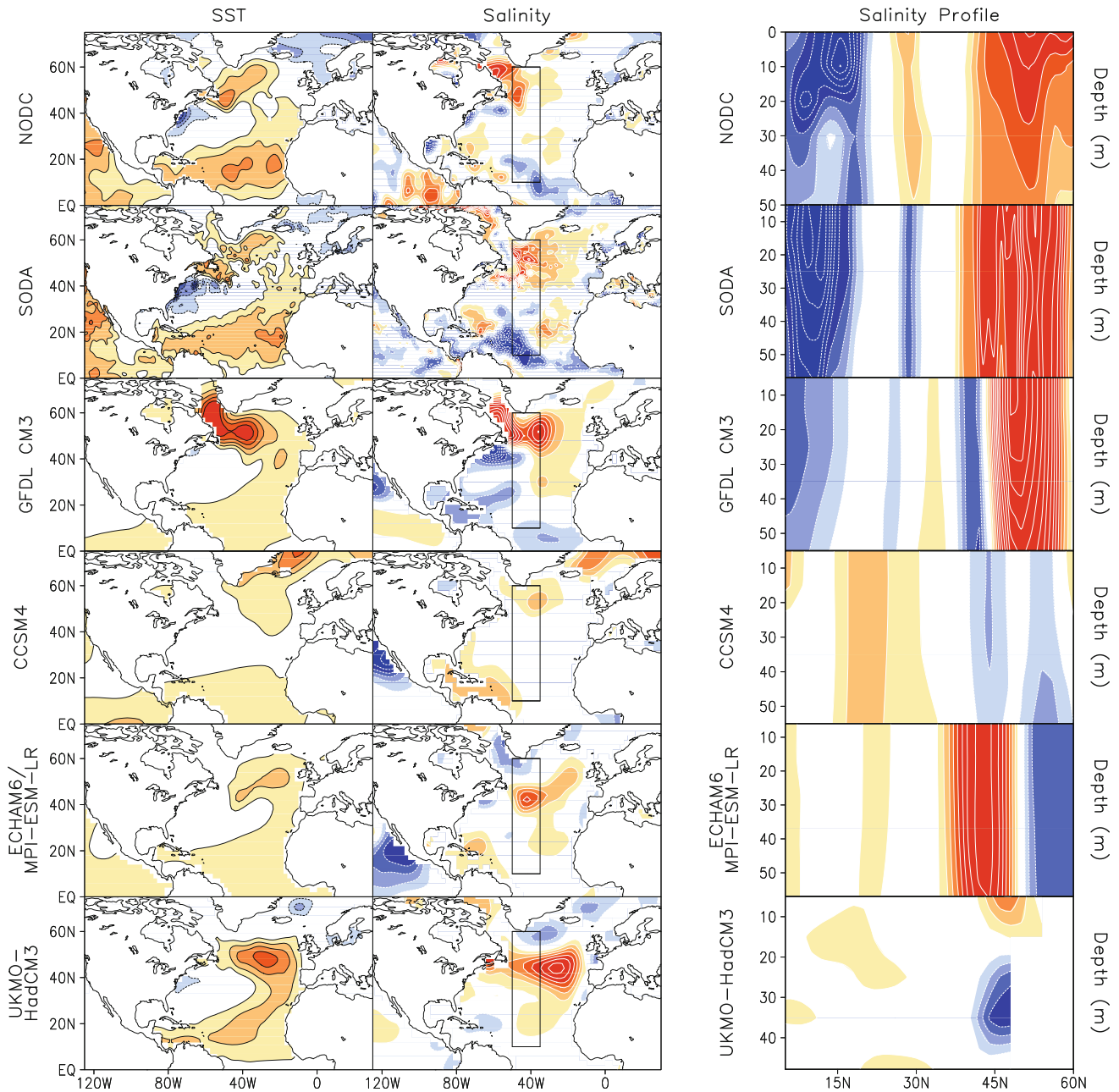


Fig. 6 All-season regressions of the smoothed AMO indices on SST and salinity for the period winter 1955–fall 1999. Regressions on SSTs are displayed in the *left-hand side panels*, on the vertically averaged (0–50 m) salinity field are displayed on the *central panels*, while on salinity latitudinal profiles are shown on the *right-hand side panels*. Regressions are calculated for each ensemble member separately and a mean value is subsequently computed and shown. *Red/blue shading* denotes positive/negative SST and salinity anomalies. The contour intervals for the maps are 0.1 K and 0.2ppt for SST

and salinity anomalies, respectively, having skipped the zero contour line. The *right-hand side panels* show latitude–depth cross-sections of the longitudinally averaged (35°–50°W) regressions of the AMO index with the 3-dimensional salinity field; the contour interval is 0.1ppt. The *upper two rows* show regression anomalies from observations by NODC and SODA 2.2.4 ocean reanalysis. The *remaining rows* show the related AMO salinity anomalies from model simulations of the twentieth century climate from GFDL-CM3, CCSM4, ECHAM6/MPI-ESM-LR and UKMO-HadCM3

before the mature warm phase of the AMO, the Atlantic is crossed by negative heat content anomalies in the mid-latitudes (~45°N), extending from the Newfoundland to the UK (along the Gulf Stream's northern extension) and

positive anomalies in the subtropics, off of the eastern US coast and along the southern tip of Greenland that reach as far as the Nordic Sea; the deep tropics are marked by cold heat content anomalies. Two years later (that is, 2 years

before the mature warm phase), the cold heat content anomalies that were crossing the mid-Atlantic earlier, have now moved to the Nordic Sea and along the eastern US coast, while the warm heat content anomalies over southern Greenland appear expanded southward. The warm anomalies off of the eastern US have moved further to the east, toward the central subtropics, at about 30°N, with a southward extension to the tropics, off of the northwest African coast. Finally, the cold anomalies that were present in the deep tropics earlier have almost disappeared.

As time evolves toward the mature phase, the positive anomalies over southern Greenland propagate southeastward along the European and African western coasts, while the subtropical warm anomalies weaken. The cold anomalies along the eastern US extend toward the central

Atlantic and the ones over the western northern tropical Atlantic are being replaced by warm anomalies. During the post-mature phases, in both the NODC and SODA maps, the cold anomalies continue to propagate toward the central mid-Atlantic; warm anomalies around the southern tip of Greenland are being displaced further to the east, allowing for cold anomalies to develop over the Labrador Sea and the Davis Strait. Furthermore, the warm link between the mid and tropical Atlantic off of the northwestern African coast is weakened. It is important to note that the SST anomalies (Fig. 6) over the Davis Strait and Labrador Sea, as well as those over the Fram Strait (northeast of Greenland) and along the coastal, eastern US, are coincident with the same sign anomalies in heat content over the same regions, not only during the mature phase (e.g., compare Fig. 6, upper two panels in left column with Fig. 7 upper

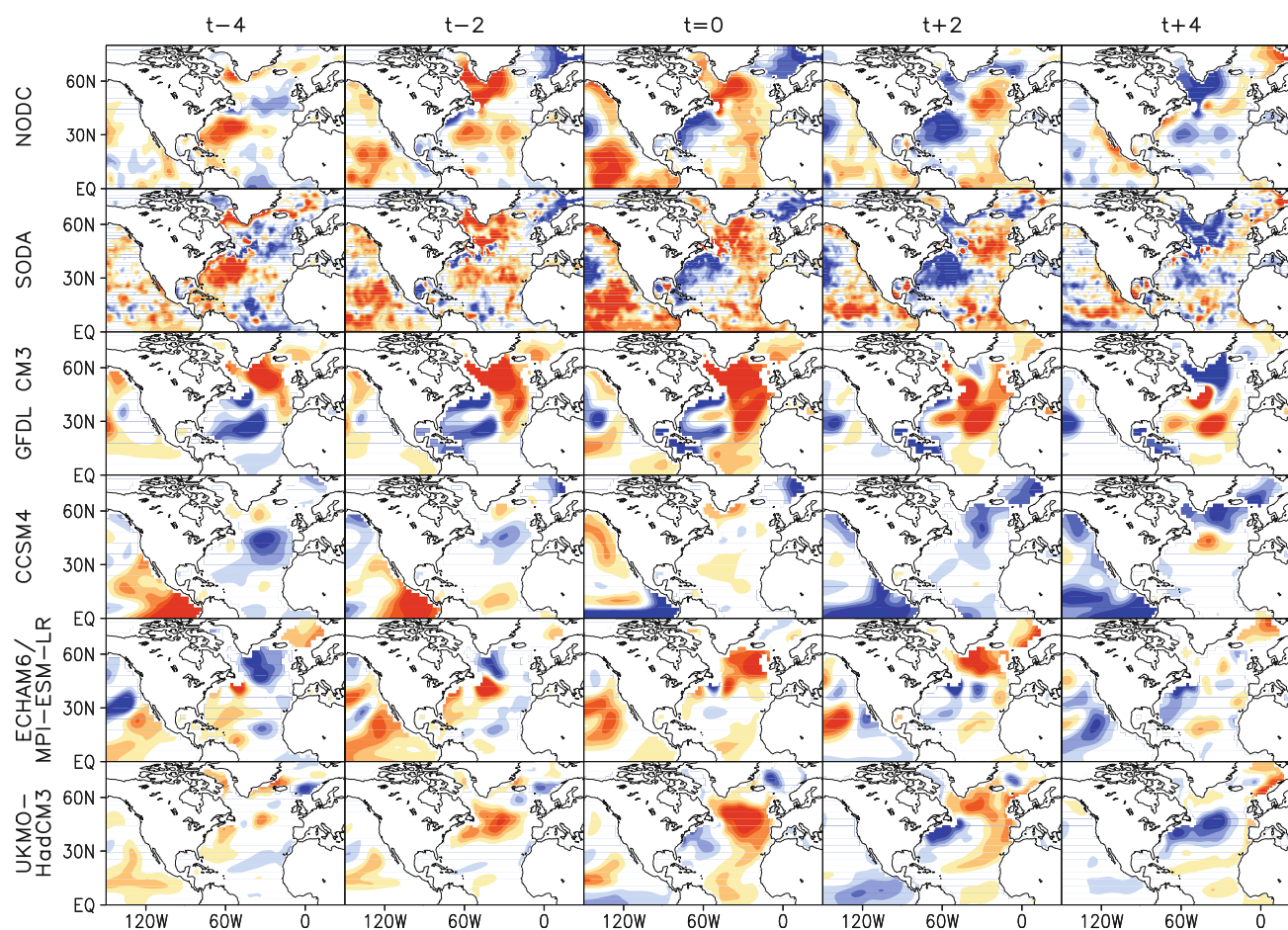


Fig. 7 All season regressions of the smoothed AMO indices on (0–400 m) vertically integrated, de-trended ocean heat content for the period, winter 1955–fall 1999. The *upper two rows* show regression anomalies from observations by NODC and by the SODA 2.2.4 ocean reanalysis, and the *remaining rows* show the related AMO heat content anomalies from model simulations of the twentieth century climate from GFDL CM3, CCSM4, ECHAM6/MPI-ESM-LR and

UKMO-HadCM3. Model regressions are calculated for each ensemble member separately, and a mean value is subsequently computed and plotted here. *Red/blue shading* denotes positive/negative anomalies; the contour interval is $5 \times 10^7 \text{ J/m}^2$. Regressions are displayed after five applications of the smth9 function in the GrADS plotting software

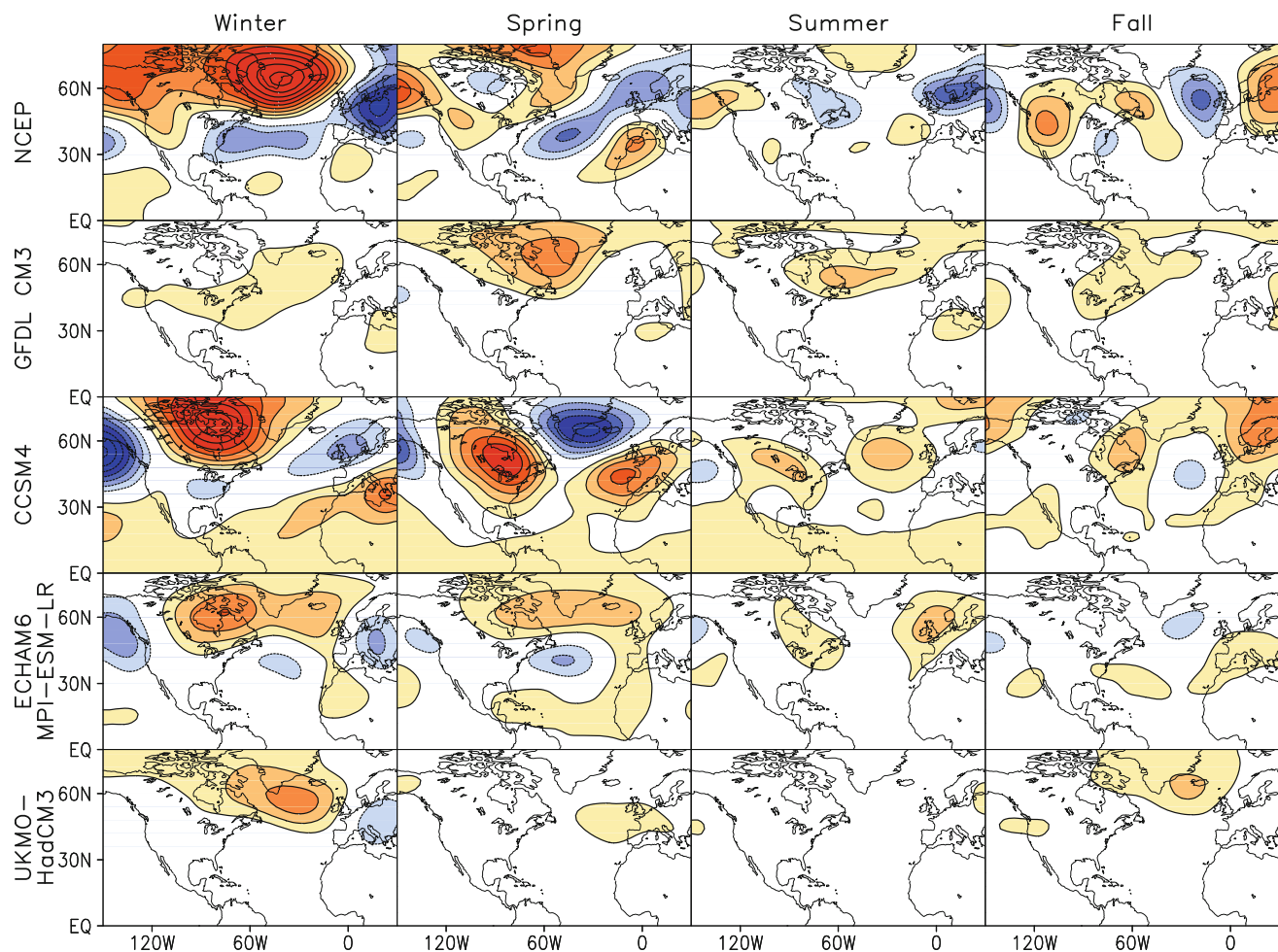


Fig. 8 Seasonal regressions of the smoothed AMO indices on 500 mb geopotential heights for the period winter 1949–fall 1999. The *upper row* was generated by regressing seasonal smoothed AMO indices from the HadISST data set on the NCEP reanalysis heights. The *remaining rows* show the related AMO height anomalies from model simulations of the twentieth century climate from GFDL CM3,

CCSM4, ECHAM6/MPI-ESM-LR and UKMO-HadCM3. Model regressions are calculated for each ensemble member separately and a mean value is subsequently computed and plotted here. *Red/blue shading* denotes positive/negative anomalies; contour interval is 4 m. Regressions are shown after two applications of the smth9 function in the GRADS plotting software

two panels in central column) but also in the pre- and post-mature phases (not shown).

GFDL-CM3 appears to be the most efficient model in capturing the spatial pattern and systematic evolution of the observed, warm and cold heat content interchanges, especially during the mature and post-mature phases. Among the other 3 models, CCSM4 lacks the ability to efficiently portray a reasonable evolution of the AMO-related, heat content anomalies, whereas UKMO-HadCM3 and ECHAM6/MPI-ESM-LR exhibit a better propagation of sub-surface temperature anomalies, with a principal focus in the northern mid-latitudes. The tropical North Atlantic in the latter two models appears more quiescent during the pre- and post-mature phases, similarly to the pre- and post-cursor periods of the SSTA evolution (not shown for this shorter period but very similar to the ones examined in Fig. 5).

3.4 AMO's atmospheric footprint

A thorough characterization of the AMO is not complete without its associated signature on the atmosphere and surface climate over the neighboring continents. Investigation of seasonality is of great importance, given the possibility of canceling/building effects that may arise from season to season throughout the year. The seasonality of AMO's influence on the overlying atmosphere is analyzed via regressions of the AMO index on the 500 mb circulation anomalies (Fig. 8). It is important to note that these simultaneous regressions include both the atmospheric weather noise (the part of atmospheric variability that does not emerge as a result of boundary or external forcing mechanisms (Schneider and Fan 2007) and AMO's atmospheric response, which tends to abate SST variability. To extract AMO's forced response in atmospheric and

other climate features (i.e., hydroclimate), one needs to remove the weather noise-related surface fluxes and variability from the observed SST evolution, as shown in Fan and Schneider (2012), by i.e., employing an interactive model configuration of a coupled GCM forced by weather noise surface fluxes, to isolate the individual contribution of local weather surface fluxes to the N. Atlantic SST variability. Such an approach could advance investigation of the mechanisms that lead to such low-frequency SST pulses, as shown in Schneider and Fan (2012).

Observations (top four panels, Fig. 8) show prominent winter geopotential height anomalies that decrease to a minimum during the summer. A resemblance to the negative NAO pattern of high pressure over the Icelandic region and a contrasting pattern of low pressure over the western Atlantic-Azores region are discernible during winter. Furthermore, the geopotential height patterns exhibit same-sign anomalies for different atmospheric levels (not shown here), indicating the existence of an equivalent barotropic structure. A supplemental feature that is worth mentioning is the high–low–high wave pattern that emerges during the fall season over the US-Labrador Sea region, with a ridge (trough) over the western (eastern) US; this is essential in relating circulation anomalies to perturbations in surface temperature and precipitation over the continental US (examined further below.)

The four models exhibit some problems while attempting to simulate the observed seasonality of the atmospheric, SST-related features and the associated regional circulation patterns. While portraying their own version of the observed winter ridge/trough over the Icelandic/western Atlantic-Azores region, most of them are unable to capture the atmospheric seasonality that is characterized by a summer minimum in the anomalies. It is revealing to find out that while GFDL-CM3 was shown to be the best model in reproducing observed features over the ocean, it is the worst in capturing the respective atmospheric patterns via geopotential height regressions; some of the key, contradictory features (with respect to observations) include maximum positive anomalies over the Icelandic region during spring rather than winter, as well as minimum height anomalies during the winter and fall seasons (instead of summer). On the other hand, CCSM4, which was the worst in simulating the observed oceanic features of the AMO, exhibits a reasonable seasonal cycle on the atmospheric front (the strongest among all models): it displays maximum (minimum) anomalies in winter (summer), but of greater amplitude in comparison to observations, including an enhanced subtropical/tropical response that is not seen in observations. The respective atmospheric features in ECHAM6/MPI-ESM-LR are marginally stronger than in GFDL-CM3, with a seasonal cycle of similar skill to the one in GFDL-CM3, however: maximum

anomalies are displayed in winter, with the strongest minimum anomalies being observed during fall. Finally, in UKMO-HadCM3 a seasonal cycle similar to the one in observations is discerned, but of much weaker amplitude: in fact, the response is so weak that it is characterized by normal conditions during the defined summer season. At last, it is worth noting that none of the models captures the fall wave pattern over North America and parts of the northeastern Atlantic; this is important as low and mid-tropospheric geopotential height variability can be related to winds and low-level circulation that is associated with moisture transport and is therefore conducive to more efficiently understanding and modeling hydroclimate changes and extreme events (i.e., droughts) over the US Great Plains and other regions (Ruiz-Barradas and Nigam 2005).

3.5 AMO and precipitation patterns

The main rainy season for the majority of the domain examined in this study occurs in the months of summer and fall, but among these seasons, fall is the season during which we observe the greatest association between the AMO and regional geopotential height anomalies, as well as circulation and surface climate features. The warm phase of the AMO is characterized by prominent SST anomalies that are linked to important precipitation anomalies in observations (Fig. 9, upper panel). The structure of the fall-SST anomalies in the mid-latitudes and northern tropical Atlantic⁵ is similar to the all-season regressed anomalies (Fig. 1) but with a stronger maximum in the mid-latitudes. The associated precipitation anomalies display a general decrease in rainfall over the US, which is particularly prominent in the eastern half⁶; furthermore, a rainfall decrease is noted over the western and southeastern portions of northern South America. On the other hand, enhanced rainfall is observed over Central America, the Guinean zone in Africa,⁷ southern Europe, and the UK (Fig. 9, upper panel). The previously studied 500 mb anomalous geopotential height pattern (ridge-trough-ridge) that is present during fall, is a good example of how mid-level circulation anomalies generate precipitation

⁵ The AMO-related SST anomalies in the North Atlantic are minimum in spring, a time when the SST anomalies over the northern tropical Atlantic reach the maximum extension and have the largest impact over northeastern Brazil during the rainy season (not shown). This is all reminiscent of the so called interhemispheric mode.

⁶ The influence of the AMO in central US rainfall is considerably less extensive in summer than in fall (not shown).

⁷ The impact of the AMO on regional rainfall over Africa depends on the season. As noted above, the Guinean zone is affected in fall, but the Sahelian zone to its north is most affected in summer (not shown).

anomalies over land: the wave pattern of high–low–high at the 500 mb pressure level over the US enables the generation of near-the-surface, northerly winds, reduced moisture transport and a low-level subsidence that can subsequently lead to enhanced dryness over the central and southeastern US.

As far as the models are concerned, fall SST anomalies manifest some similarities to the all-season regressions, with some distinct differences, however, due to the seasonality of the phenomenon (Fig. 9, middle and lower panels). As in the case of the all-season regressions, models

(with the exception of GFDL-CM3) tend to place the maximum SST anomalies in the North Atlantic too far to the east of the Labrador Sea, in comparison to observations. CCSM4 is the only model with no subtropical/tropical extension of the SST anomalies; on the other hand, GFDL-CM3 and ECHAM6/MPI-ESM-LR demonstrate a similar-magnitude, subtropical/tropical extension of the North Atlantic SST anomalies (as in observations), a phenomenon that was absent from the all-season regressions. Finally, UKMO-HadCM3's fall SSTA structure appears similar to the all-season one, remaining unable to match the

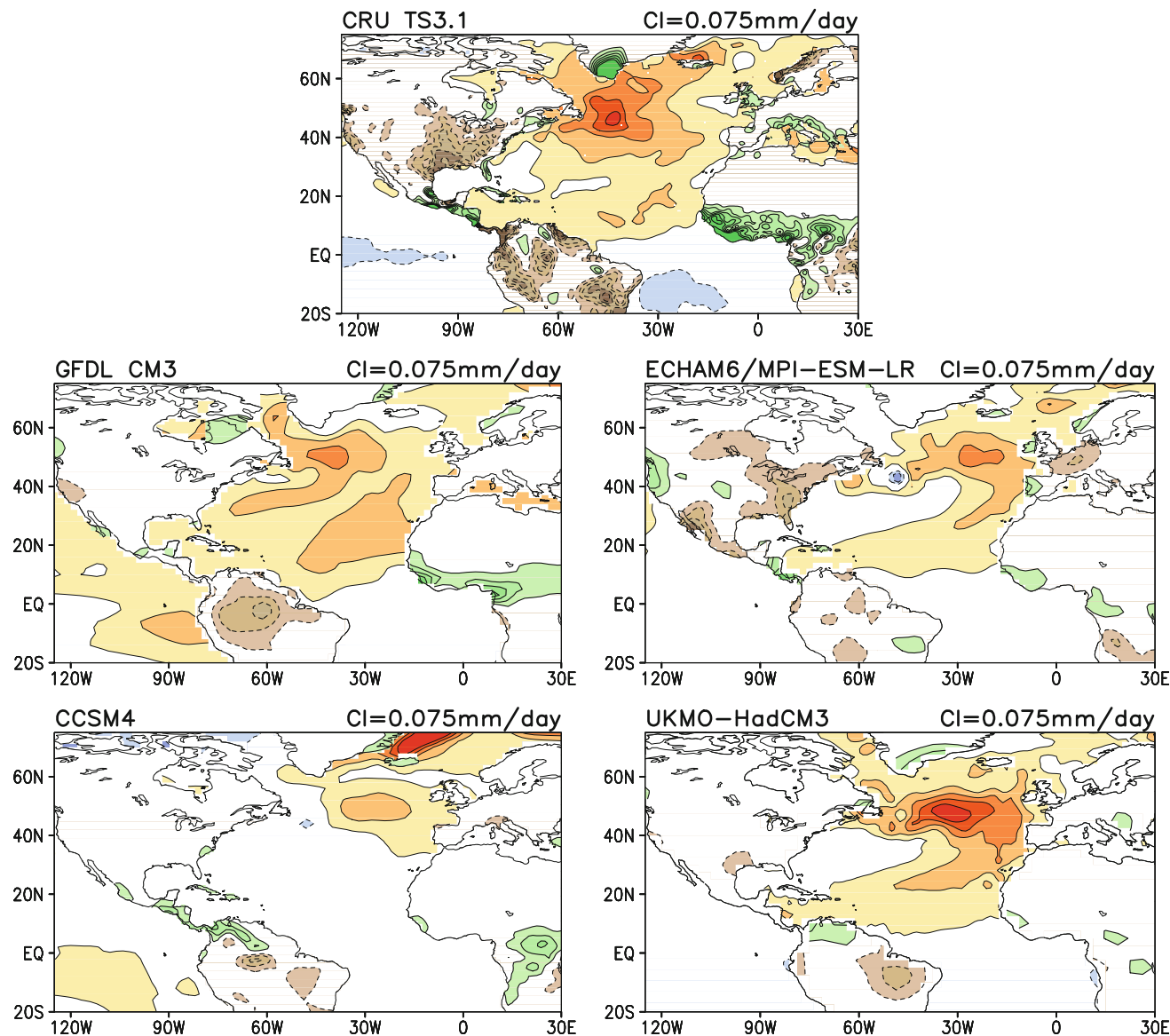


Fig. 9 Fall regressions of smoothed AMO indices on SST and precipitation for the winter 1901–fall 1999 time period. The *upper panel* shows the regression of the observed HadISST smoothed AMO index on its own SSTs and CRUTS3.1 precipitation. The *remaining panels* show the related AMO SST and precipitation anomalies from model simulations of the twentieth century climate from GFDL-CM3,

CCSM4, ECHAM6/MPI-ESM-LR and UKMO-HadCM3. Regressions are calculated for each ensemble member separately and an average is subsequently calculated and shown here. *Blue/red* and *green/brown* denote positive/negative anomalies for SST and precipitation fields, respectively; contour intervals are 0.075 mm/day and 0.1 K, respectively

observed magnitude of the SSTA extension into the Tropics.

Now the four models remain challenged when focusing on their ability to capture the vast hydroclimate features that are related to the warm phase of the AMO, during fall. The observation-based, reduced rainfall in central and eastern US is only partially captured by ECHAM6/MPI-ESM-LR and in a minimum way by UKMO-HadCM3. On the other hand, the reduced rainfall over South America is broadly captured by GFDL-CM3 in its western portion, with CCSM4 and UKMO-HadCM3 having only a few hints of the reduced rainfall over its southeastern part. The broad region of enhanced rainfall over the Guinean zone in Africa is also problematic for all four models; while GFDL-CM3 portrays decreased rainfall over the region, accompanied with enhanced rainfall over the Sahelian zone (extending too far to the north, however, with respect to observations), the other three models are unable to simulate the magnitude and spatial extent of these precipitation anomalies.

3.6 AMO-related, surface air temperature variability

Given the decadal scale of the phenomenon, it is also important to identify AMO's signal in surface air temperature, in order to differentiate it from the man-induced impact on regional temperatures. Regressions of the AMO indices on surface air temperature during fall are shown in Fig. 10. Warming associated with the warm phase of the AMO in observations is manifested over the western US, the Labrador Peninsula and southern Greenland, large parts of Europe, northwestern Africa, as well as western South America (Fig. 10, upper panel). The AMO influence on surface air temperature is seasonally dependent: while fall is the season with the most extended warming over the domain used for the current study, winter is the season when warming appears to be maximum over eastern US and Canada, with a generalized cooling observed over Europe, except for a region of intense warming occurring over the Scandinavian Peninsula (not shown).

AMO-related fall surface air temperature anomalies are not being fully captured, in magnitude or position, by any of the four model simulations employed here. The warming over western US is only timidly shown by ECHAM6/MPI-ESM-LR. The remaining models (with the exception of CCSM4) weakly portray the warming over the Labrador Peninsula and southern Greenland. In addition, the broad extension of the warming over northwestern Africa is also weakly and sparsely simulated by all four models. Finally, the warming over western South America appears exaggerated by GFDL-CM3, with an extent that surpasses the one in observations, while ECHAM6/MPI-ESM-LR depicts the warming in a muted way.

4 Summary and discussion

The basin-wide, sea surface temperature variability known as the Atlantic Multidecadal Oscillation and its signature on surface and sub-surface fields, as well as its impact on the climate of neighboring continents, has been analyzed in this study, in an effort to construct an integrated view of the phenomenon. North Atlantic SSTs exert a significant and oftentimes predictable influence on climate, with devastating socioeconomic impacts, such as the ones derived from multi-year drought and enhanced rainfall incidents over N. America. Thus, the characterization of the AMO is of vital significance in assessing the efficiency of decadal climate prediction experiments of current state-of-the-art models participating in the CMIP5 project. The need for a proper incorporation of such low frequency natural variability phenomena, such as the AMO, has been noted in past studies (Meehl et al. 2009; Hurrell et al. 2009; Nigam et al. 2011) and is essential for a better attribution of natural and human-induced effects in model projections of present and future climate events.

A clarified description of AMO's spatiotemporal structure and evolution emerges from century-long observations. The mature warm phase of the smoothed AMO is associated with warm anomalies in the North Atlantic mid-latitudes over the sub-polar gyre region and the Labrador sea and a secondary maximum of warm anomalies in the northern tropical Atlantic (also see Nigam et al. 2011). The relative magnitude of the maximum SST anomalies is inverted when the analysis is confined to the second half of the twentieth century, despite the fact that the structure remains unchanged.

A period of 58 years is inferred for the smoothed AMO from observations, which is smaller than other estimations in the 65–75 years range (e.g., Enfield et al. 2001; Sutton and Hodson 2005); these other estimates are based on the use of heavy smoothing of the area-averaged anomalies, as compared with the 1-2-1 binomial filter used here. Spectral analysis shows that oscillations in the 70–80 year range are dominant in the observed smoothed AMO index, but are combined with oscillations in the 30–40 year range and shorter periods. Models, however, underestimate the life span of the phenomenon by increasing variability in the 10–20 year range, to the extent that it becomes more dominant than variability in the 70–80 year range.

Sea surface temperature anomalies are shown to be associated with vertically-integrated heat content anomalies (sfc-400 m) that evolve coherently in time, as well as vertically integrated (sfc.-50 m) salinity anomalies—particularly the positive anomalies developing over the Labrador Sea and the negative ones off of the US coast. While this configuration of SST/salinity/heat content anomalies over the deep water formation region of the sub-polar gyre

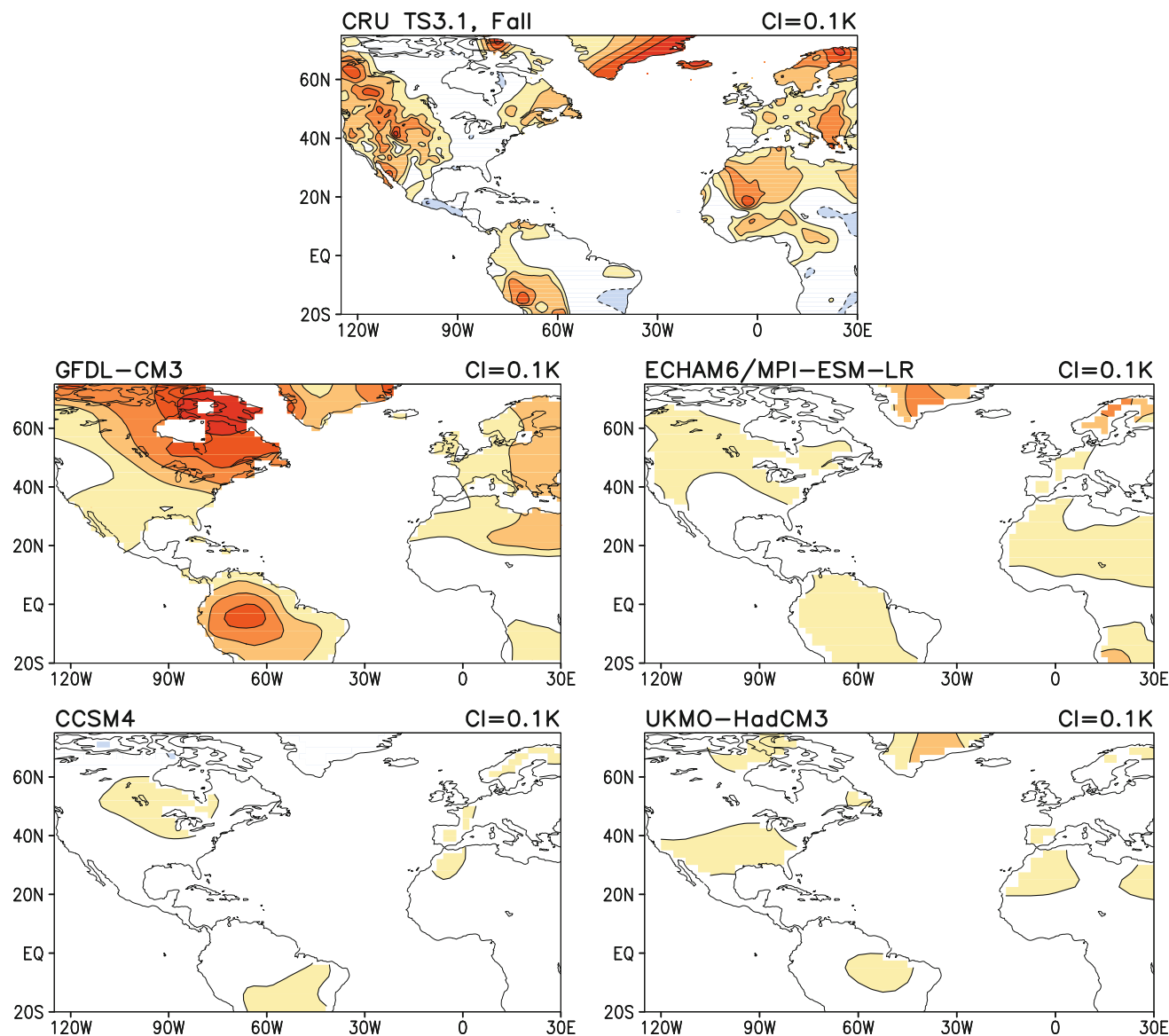


Fig. 10 Fall regressions of smoothed AMO indices on surface air temperature for the winter 1901–fall 1999 time period. The *upper panel* shows the regression of the observed HadISST smoothed AMO index on CRUTS3.1 surface air temperature. The *remaining panels* show the related air temperature anomalies from model simulations of

the twentieth century climate from GFDL CM3, CCSM4, ECHAM6/MPI-ESM-LR and UKMO-HadCM3. Regressions are calculated for each ensemble member separately and an average is subsequently calculated and shown here. *Blue/red* denotes positive/negative anomalies; contour interval is 0.1 K

points toward a more active thermohaline circulation during the warm phase of the AMO, the cold phase of the AMO suggests a weaker thermohaline circulation and fresh water anomalies, similar to the ones evolving during Great Salinity Anomaly events (as noted in Slonosky et al. 1997). An atmospheric signal associated with the N. Atlantic low-frequency variability is also discerned from observations, when looking at regressions of the seasonal AMO index on the respective 500 mb geopotential height field. Regional geopotential height anomalies, including both the weather noise that is forcing the SSTA evolution, as well as the atmospheric feedback to the Atlantic impact, appear

stronger in winter and weaker during summer, while persisting, however, throughout the entire year, as noted in Kushnir et al. (2010) and Wang et al. (2010). The fall season appears to be of critical importance as far as the interactions between the AMO and the regional surface climate of the adjacent continents are concerned; an anomalous wave pattern extending from North America to eastern Europe is linked to reduced (enhanced) rainfall over large portions of the Americas (western Africa, over the Guinean region) and generalized warming over the western Americas, Greenland, Europe and northwestern Africa, during that season.

The four CMIP5 models examined in this study capture the focus of North Atlantic SSTAs in the mid-latitudes, while moving, however, the maximum anomalies further to the east than observations indicate, and while remaining, in general, unable to portray the extension of same-sign anomalies into the tropics, during the pre- and post-mature phases of the AMO. The characteristic period of the AMO remains underestimated with an error range between 6 (UKMO-HadCM3) and 18 years (ECHAM6/MPI-ESM-LR). UKMO HadCM3 appears to be most successful in simulating the AMO's spatial evolution and variability around the mature phase (± 4 years). Furthermore, the models tend to associate N. Atlantic SST anomalies (especially the warm ones) with the sfc-400 m heat content variations (as seen in observations), while appearing more challenged, however, when simulating the observed temporal evolution of these anomalies close to the mature phase of the AMO. At the mature phase, GFDL-CM3 and UKMO-HadCM3 portray some of the observed features (of the SST and heat content fields), such as the contrasting warm anomalies over the sub-polar gyre region (Labrador Sea and Davis Strait) and the cold anomalies off of the eastern US coastline. GFDL-CM3 is the only model capturing the spatial distribution of the salinity anomalies, while exaggerating, however, their spatial extent off of the US coast. In general, GFDL-CM3 exhibits the most favorable oceanic description associated with the AMO, while CCSM4 exhibits the least favorable one (CCSM4 salinity and heat content anomalies are the weakest among models, and have the least resemblance to the observed structure).

None of the four models employed in this study is able to capture the anomalous circulation pattern that is seen in observations during the fall season. CCSM4, despite its unsuccessful depiction of the AMO-related, oceanic features, displays a more realistic atmospheric structure (in comparison to the other models) via the seasonality of the 500 mb geopotential heights. Regarding the fall hydroclimate characteristics associated with the AMO, ECHAM6/MPI-ESM-LR is best at representing the reduced rainfall over the US (although it is deficient in capturing its spatial extent); over the same region, UKMO-HadCM3 displays similar to the observations but of minimum amplitude features, whereas CCSM4 and GFDL-CM3 are unable to reproduce the reduced precipitation impact, manifesting normal and increased precipitation patterns, respectively. Finally, regarding the AMO-related, surface air temperature anomalies, GFDL-CM3 demonstrates the strongest, warming signal among the models but is unable to capture the warming over western North America, while ECHAM6/MPI-ESM-LR marginally captures the extensive warming; CCSM4 and UKMO-HadCM3 are only able to represent the warming over northwestern Africa, in a

minimum way. One can therefore argue that representation of low frequency variability and its associated hydroclimate structure remains challenged in these simulations and that there is an uneven (incoherent) progress noted between these models and their respective predecessors (their CMIP3 versions), as noted in recent studies (Ting et al. 2011; Ruiz-Barradas et al. 2012). Furthermore, the models remain unable to efficiently depict a holistic perspective of the AMO-related oceanic and atmospheric features. More research is therefore necessary to unravel potential mechanisms that are critical in low frequency variability structure and evolution in the North Atlantic and that might not be well represented in models, hindering thus their ability to more efficiently portray the observed, AMO signature. Such mechanisms include the ability of climate models (or lack thereof) to a. efficiently produce the Pacific basin link of the Atlantic impact (Ting et al. 2011; Guan and Nigam 2009)—this connection has been noted in several studies in the past (Enfield and Mayer 1997; Ruiz-Barradas et al. 2000; Latif 2001), b. to capture the role of the ocean in long-term variability (i.e., by efficiently simulating its surface and sub-surface structure), c. to understand and simulate the coupling between the ocean and the overlying atmosphere and the connection between circulation features, weather noise (momentum, heat, freshwater) and ocean-induced surface fluxes (via the atmospheric response to SST evolution) and regional hydroclimate (for instance, the relation between the recent N. American drought events of 2012 in the context of North Atlantic and equatorial and northern Pacific impact). Some research questions that arise from the current study and are yet to be fully answered include: a. the connection between the region of origin, the excitation mechanism and the propagation of salinity anomalies between the Arctic and N. Atlantic basins (Sundby and Drinkwater 2002) and the ways in which these anomalies relate to low-frequency, sea surface temperature variability in the N. Atlantic and b. the relative contribution of the surface versus deeper layers of the ocean to the increase in oceanic heat content and the ways in which this relates to the spatiotemporal pattern of multi-decadal, N. Atlantic SST variability.

5 Conclusions

To conclude, we believe that our analysis sheds light on the structure and evolution of the low-frequency AMO, while also inciting supplemental interest for AMO's footprint on both surface and sub-surface variables. The modeled AMO image that emerges via the newly released historical simulations demonstrates limited success, particularly on the continental climate impact front. A greater focus on building AMO's sub-surface signature, throughout the

entire North Atlantic basin and its co-variability with salinity and meridional overturning circulation fluctuations could potentially help improve the incorporation of AMO-related mechanisms in climate models. However, this may not be enough to substantially advance the way the atmosphere responds to mid-latitude sea surface temperature anomalies in the models. Without a proper incorporation of low-frequency natural variability in climate simulations, decadal predictability and the accuracy of climate projections under different climate change scenarios remain compromised.

Acknowledgments The authors wish to acknowledge support from the NOAA grant NA10OAR4310158. They also wish to thank Dr. Edwin K. Schneider, Executive Editor at Climate Dynamics and two anonymous reviewers for their constructive comments and insightful references that helped improve the paper, as well as Jose Caceres, Assistant System Administrator at University of Maryland, for providing help with respect to data access from the Earth System Grid (ESG) website. Finally, they wish to acknowledge the World Climate Research Programme's Working Group on Coupled Modelling, which is responsible for CMIP, and wish to thank the climate modeling groups used in this paper for producing and making available their model output. For CMIP, the U.S. Department of Energy's Program for Climate Model Diagnosis and Intercomparison provides coordinating support and led development of software infrastructure in partnership with the Global Organization for Earth System Science Portals.

References

- Bjerknes J (1964) Atlantic air–sea interaction. *Advances in geophysics*, vol 10. Academic Press, London, pp 1–82
- Booth B et al (2012) Aerosols implicated as a prime driver of twentieth-century North Atlantic climate variability. *Nature* 484:228–232. doi:10.1038/nature10946
- Boyer TP, Levitus S, Antonov J, Locarnini R, Garcia H (2005) Linear trends in salinity for the World Ocean, 1955–1998. *Geophys Res Lett* 32:L01604. doi:10.1029/2004GL021791
- Carton J, Giese B, Grodsky S (2005) Sea level rise and the warming of the oceans in the SODA ocean reanalysis. *J Geophys Res* 110:C09006. doi:10.1029/2004JC002817
- Chu PC (2011) Global upper ocean heat content and climate variability. *Ocean Dyn* 61(8):1189–1204
- Deser C, Blackmon ML (1993) Surface climate variations over the North Atlantic Ocean during winter: 1900–89. *J Clim* 6:1743–1753. doi:10.1175/1520-0442(1993)006<1743:SCVOTN>2.0.CO;2
- Deser C, Holland M, Reverdin G, Timlin M (2002) Decadal variations in Labrador Sea ice cover and North Atlantic sea surface temperatures. *J Geophys Res* 107(C5). doi:10.1029/2000JC000683
- Enfield C, Cid-Serrano L (2006) Projecting the risk of future climate shifts. *Int. J. Climatol* 26:885–895. doi:10.1002/joc.1293
- Enfield DB, Mayer DA (1997) Tropical Atlantic sea surface temperature variability and its relation to El Niño–Southern Oscillation. *J Geophys Res* 102(C1):929–945. doi:10.1029/96JC03296
- Enfield D, Mestas-Nunez E, Trimble P (2001) The Atlantic multidecadal oscillation and its relation to rainfall and river flows in the continental US. *Geophys Res Lett* 28:2077–2080
- Evan AT et al (2009) The role of aerosols in the evolution of Tropical North Atlantic Ocean temperature anomalies. *Science* 324(5928):778–781. doi:10.1126/science.1167404
- Fan M, Schneider EK (2012) Observed decadal North Atlantic tripole SST variability. Part I: weather noise forcing and coupled response. *J Atmos Sci* 69:35–50. doi:10.1175/JAS-D-11-018.1
- Frankcombe LM (2010) The Atlantic multidecadal oscillation in models and observations. *Natuur- en Sterrenkunde Proefschriften*. <http://igitur-archive.library.uu.nl/dissertations/2010-0617-200232/UUindex.html>
- Gelderloos R, Straneo F, Katsman CA (2012) Mechanisms behind the Temporary shutdown of deep convection in the Labrador Sea: lessons from the great salinity anomaly years 1968–71. *J Clim* 25:6743–6755. doi:10.1175/JCLI-D-11-00549.1
- Guan B, Nigam S (2009) Analysis of Atlantic SST variability factoring interbasin links and the secular trend: clarified structure of the Atlantic multidecadal oscillation. *J Clim* 22:4228–4239. doi:10.1175/2009JCLI2921.1
- Hansen JE et al (2005) Earth's energy imbalance: confirmation and implications. *Science* 308:1431–1435. doi:10.1126/science.1110252
- Hodson D, Sutton R, Cassou C, Keenlyside N, Okumura Y, Zhou T (2010) Climate impacts of recent multidecadal changes in Atlantic Ocean sea surface temperature: a multimodel comparison. *Clim Dyn* 34:1041–1058. doi:10.1007/s00382-009-0571-2
- Huang B et al (2011) Influences of tropical–extratropical interaction on the multidecadal AMOC variability in the NCEP climate forecast system. *Clim Dyn* 39(3–4):531–555. doi:10.1007/s00382-011-1258-z
- Hurrell JW et al (2009) Decadal climate prediction: opportunities and challenges. Community White Paper, *OceanObs'09* <https://abstracts.congrx.com/scripts/jmevent/abstracts/fcxnl-09a02a-1661836-1-decadalprediction.final.pdf>
- Kalnay E et al (1996) The NCEP/NCAR 40-year reanalysis project. *Bull Am Meteorol Soc* 77:437–470
- Keenlyside NS, Latif M, Jungclaus J, Kornblueh L, Roeckne E (2008) Advancing decadal-scale climate prediction in the North Atlantic sector. *Nature* 453:84–88
- Kelly KA, Dong S (2004) The relationship of western boundary current heat transport and storage to mid-latitude ocean–atmosphere interaction. In: Wang C, Xie S-P, Carton JA (eds) *Earth's climate: the ocean–atmosphere interaction*. pp 347–363, American Geophysical Union Geophysical Monograph 147
- Kerr RA (2000) A North Atlantic climate pacemaker for the centuries. *Science* 288(5473):1984–1986. doi:10.1126/science.288.5473.1984
- Knight J, Folland C, Scaife A (2006) Climate impacts of the Atlantic multidecadal oscillation. *Geophys Res Lett* 33:L17706. doi:10.1029/2006GL026242
- Kushnir Y (1994) Interdecadal variations in North Atlantic sea surface temperature and associated atmospheric conditions. *J Clim* 7:141–157
- Kushnir Y, Seager R, Ting M, Naik N, Nakamura J (2010) Mechanisms of tropical Atlantic SST influence on North American precipitation variability. *J Clim* 23:5610–5628
- Latif M (2001) Tropical Pacific/Atlantic Ocean interactions at multidecadal time scales. *Geophys Res Lett* 28:539–542
- Latif M et al (2004) Reconstructing, monitoring, and predicting decadal-scale changes in the North Atlantic thermohaline circulation with sea surface temperature. *J Clim* 17:1605–1614
- Levitus S, Antonov J, Boyer TP, Stephens C (2000) Warming of the world ocean. *Science* 287:2225–2229
- Levitus S, Antonov JL, Wang J, Delworth TL, Dixon KW, Broccoli AJ (2001) Anthropogenic warming of Earth's climate system. *Science* 292:267–270

- Levitus S, Antonov J, Boyer T (2005) Warming of the world ocean, 1955–2003. *Geophys Res Lett* 32:L02604. doi:[10.1029/2004GL021592](https://doi.org/10.1029/2004GL021592)
- Lozier MS, Leadbetter S, Williams RG, Roussenov V, Reed MSC, Moore NJ (2008) The spatial pattern and mechanisms of heat-content change in the North Atlantic. *Science* 319:800–803. doi:[10.1126/science.1146436](https://doi.org/10.1126/science.1146436)
- Mann ME, Emanuel KA (2006) Atlantic hurricane trends linked to climate change. *Eos* 87(24):233–244
- Medhaug I, Furevik T (2011) North Atlantic 20th century multidecadal variability in coupled climate models: sea surface temperature and ocean overturning circulation. *Ocean Sci Discuss* 8:353–396. doi:[10.5194/osd-8-353-2011](https://doi.org/10.5194/osd-8-353-2011)
- Meehl G, Tebaldi C, Walton G., Easterling D, McDaniel L (2009) Relative increase of record high maximum temperatures compared to record low minimum temperatures in the U.S. *Geophys Res Lett* 36:L23701. doi:[10.1029/2009GL040736](https://doi.org/10.1029/2009GL040736)
- Meinshausen M et al (2011) The RCP greenhouse gas concentrations and their extension from 1765 to 2300. *Clim Change* 109: 213–241. doi:[10.1007/s10584-011-0156-z](https://doi.org/10.1007/s10584-011-0156-z)
- Mitchell TD, Jones PD (2005) An improved method of constructing a database of monthly climate observations and associated high-resolution grids. *Int J Climatol* 25:693–712. doi:[10.1002/joc.1181](https://doi.org/10.1002/joc.1181)
- Nigam S, Guan B, Ruiz-Barradas A (2011) Key role of the Atlantic multidecadal oscillation in 20th century drought and wet periods over the Great Plains. *Geophys Res Lett* 38:L16713. doi:[10.1029/2011GL048650](https://doi.org/10.1029/2011GL048650)
- Polyakov IV, Bhatt US, Simmons HL, Walsh D, Walsh JE, Zhang X (2005a) Multidecadal variability of North Atlantic temperature and salinity during the twentieth century. *J Clim* 18:4562–4581
- Polyakov IV et al (2005b) One more step toward a warmer Arctic. *Geophys Res Lett* 32:L17605. doi:[10.1029/2005GL023740](https://doi.org/10.1029/2005GL023740)
- Quenouille MH (1952) *Associated measurements*. Academic, New York
- Rayner NA et al (2005) Improved analyses of changes and uncertainties in sea surface temperature measured in situ since the mid-nineteenth century: the HadSST2 dataset. *J Clim* 19:446–468
- Reverdin G, Cayan D, Kushnir Y (1997) Decadal variability of hydrography in the upper northern North Atlantic in 1948–1990. *J Geophys Res* 102(C4). doi:[10.1029/96JC03943](https://doi.org/10.1029/96JC03943)
- Ruiz-Barradas A, Nigam S (2005) Warm-season rainfall variability over the US Great Plains in observations, NCEP and ERA-40 reanalyses, and NCAR and NASA atmospheric model simulations. *J Clim* 18:1808–1830
- Ruiz-Barradas A, Carton JA, Nigam S (2000) Structure of interannual-to-decadal climate variability in the tropical Atlantic sector. *J Clim* 13:3285–3297. doi:[10.1175/1520-0442](https://doi.org/10.1175/1520-0442)
- Ruiz-Barradas A, Nigam S, Kavvada A (2012) The Atlantic multidecadal oscillation in 20th century climate simulations: uneven progress from CMIP3 to CMIP5. *Clim Dyn. Major Revisions*
- Schneider EK, Fan M (2007) Weather noise forcing of surface climate variability. *J Atmos Sci* 64:3265–3280. doi:[10.1175/JAS4026.1](https://doi.org/10.1175/JAS4026.1)
- Schneider EK, Fan M (2012) Observed decadal North Atlantic tripole SST variability. Part II: diagnosis of mechanisms. *J Atmos Sci* 69:51–64. doi:[10.1175/JAS-D-11-019.1](https://doi.org/10.1175/JAS-D-11-019.1)
- Slonosky VC, Mysak LA, Derome J (1997) Linking Arctic sea-ice and atmospheric circulation anomalies on interannual and decadal timescales. *Atmos Ocean* 35:333–366. doi:[10.1080/07055900.1997.9649596](https://doi.org/10.1080/07055900.1997.9649596)
- Smith TM, Reynolds RW, Peterson TC, Lawrimore J (2008) Improvements to NOAA's historical merged land–ocean surface temperature analysis (1880–2006). *J Clim* 21:2283–2296. doi:[10.1175/2007JCLI2100.1](https://doi.org/10.1175/2007JCLI2100.1)
- Sundby S, Drinkwater K (2002) On the mechanisms behind salinity anomaly signals of the northern North Atlantic. *Prog Oceanogr* 73(2):190–202
- Sutton R, Hodson D (2003) Influence of the Ocean on North Atlantic climate variability 1871–1999. *J Clim* 16:3296–3313. doi:[10.1175/1520-0442\(2003\)016<3296:IOTOON>2.0.CO;2](https://doi.org/10.1175/1520-0442(2003)016<3296:IOTOON>2.0.CO;2)
- Sutton R, Hodson D (2005) Atlantic Ocean forcing of North American and European summer climate. *Science* 309:115–117. doi:[10.1126/science.1109496](https://doi.org/10.1126/science.1109496)
- Taylor K, Stouffer R, Meehl G (2012) An overview of CMIP5 and the experiment design. *Bull Am Meteorol Soc* 93:485–498. doi:[10.1175/BAMS-D-11-00094.1](https://doi.org/10.1175/BAMS-D-11-00094.1)
- Ting M, Kushnir Y, Seager R, Li C (2009) Forced and internal twentieth-century SST trends in the North Atlantic. *J Clim* 22:1469–1481. doi:[10.1175/2008JCLI2561.1](https://doi.org/10.1175/2008JCLI2561.1)
- Ting M, Kushnir Y, Seager R, Li C (2011) Robust features of the Atlantic multi-decadal variability and its climate impacts. *Geophys Res Lett* 38:L17705. doi:[10.1029/2011GL048712](https://doi.org/10.1029/2011GL048712)
- Wang H, Fu R, Kumar A, Li WH (2010) Intensification of summer rainfall variability in the southeastern United States during recent decades. *J Hydrometeorol* 11:1007–1018
- Webster PJ, Holland GJ, Curry JA, Chang H-R (2005) Changes in tropical cyclone number, duration and intensity in a warming environment. *Science* 309:1844–1846
- Zhang R (2007) Anticorrelated multidecadal variations between surface and subsurface tropical North Atlantic. *Geophys Res Lett* 34:L12713. doi:[10.1029/2007GL030225](https://doi.org/10.1029/2007GL030225)
- Zhang R, Delworth T (2006) Impact of Atlantic multidecadal oscillations on India/Sahel rainfall and Atlantic hurricanes. *Geophys Res Lett* 33:L17712. doi:[10.1029/2006GL026267](https://doi.org/10.1029/2006GL026267)
- Zhang R, Vallis GK (2006) Impact of great salinity anomalies on the low-frequency variability of the North Atlantic climate. *J Clim* 19:470–482